Icarus 332 (2019) 50–65

Contents lists available at ScienceDirect

Icarus

journal homepage: www.elsevier.com/locate/icarus

# Shock physics mesoscale modeling of shock stage 5 and 6 in ordinary and enstatite chondrites

Juulia-Gabrielle Moreau[a,*], Tomas Kohout[a,b], Kai Wünnemann[c], Patricie Halodova[d], Jakub Haloda[e,f]

[a] Department of Geosciences and Geography, University of Helsinki, Finland
[b] Institute of Geology, The Czech Academy of Sciences, Prague, Czech Republic
[c] Museum für Naturkunde, Leibniz Institute for Evolution and Biodiversity Science, Berlin, Germany
[d] Centrum výzkumu Řež, Husinec-Řež, Czech Republic
[e] Czech Geological Survey, Prague, Czech Republic
[f] Oxford Instruments NanoAnalysis, Bucks, United Kingdom

ARTICLE INFO

*Keywords:*
Ordinary chondrites
Shock-darkening
Shock metamorphism
Mesoscale modeling
iSALE

ABSTRACT

Shock-darkening, the melting of metals and iron sulfides into a network of veins within silicate grains, altering reflectance spectra of meteorites, was previously studied using shock physics mesoscale modeling. Melting of iron sulfides embedded in olivine was observed at pressures of 40–50 GPa. This pressure range is at the transition between shock stage 5 (C−S5) and 6 (C−S6) of the shock metamorphism classification in ordinary and enstatite chondrites. To better characterize C−S5 and C−S6 with a mesoscale modeling approach and assess post-shock heating and melting, we used multi-phase (i.e. olivine/enstatite, troilite, iron, pores, and plagioclase) meshes with realistic configurations of grains. We carried out a systematic study of shock compression in ordinary and enstatite chondrites at pressures between 30 and 70 GPa. To setup mesoscale sample meshes with realistic silicate, metal, iron sulfide, and open pore shapes, we converted backscattered electron microscope images of three chondrites. The resolved macroporosity in meshes was 3–6%. Transition from shock C−S5 to C−S6 was observed through (1) the melting of troilite above 40 GPa with melt fractions of ~0.7–0.9 at 70 GPa, (2) the melting of olivine and iron above 50 GPa with melt fraction of ~0.001 and 0.012, respectively, at 70 GPa, and (3) the melting of plagioclase above 30 GPa (melt fraction of 1, at 55 GPa). Post-shock temperatures varied from ~540 K at 30 GPa to ~1300 K at 70 GPa. We also constructed models with increased porosity up to 15% porosity, producing higher post-shock temperatures (~800 K increase) and melt fractions (~0.12 increase) in olivine. Additionally we constructed a pre-heated model to observe post-shock heating and melting during thermal metamorphism. This model presented similar results (melting) at pressures 10–15 GPa lower compared to the room temperature models. Finally, we demonstrated dependence of post-shock heating and melting on the orientation of open cracks relative to the shock wave front. In conclusion, the modeled melting and post-shock heating of individual phases were mostly consistent with the current shock classification scheme (Stöffler et al., 1991, 2018).

## 1. Introduction

The partial melting of opaque iron sulfides and FeNi metals (referred as 'metals' in following text), migrating into silicate cracks, and the darkening of the lithology, has been subject to several studies (Heymann, 1967; Britt et al., 1989; Britt and Pieters, 1989, 1994; Keil et al., 1992; Kohout et al., 2014; Moreau et al., 2017, 2018). This so-called shock-darkening effect is well observed in the impact breccia of the Chelyabinsk LL5 chondrite (Kohout et al., 2014; Trieloff et al., 2017), which exhibits three distinct lithologies: a light-colored lithology (shock stage 4, C−S4, Stöffler et al., 1991), a dark-colored lithology (shock-darkened, starting from ~40 GPa, Moreau et al., 2017), and an impact-melt lithology (dark, C−S7). Shock-darkening is also characterized by the presence of localized mixed melt veins or pockets of silicates, metals and iron sulfides (Stöffler et al., 1991, 2018) and is related to shock metamorphism (e.g. Stöffler et al., 1991, 2018; Rubin et al., 1997; Fritz et al., 2017; Bischoff et al., 2018) as described in Rubin (1992), Bennett and McSween (1996), or Wang et al. (2011).

* Corresponding author at: P.O. Box 64, FI-00014, University of Helsinki, Finland.
*E-mail address:* juulia.moreau@helsinki.fi (J.-G. Moreau).

https://doi.org/10.1016/j.icarus.2019.06.004
Received 6 September 2018; Received in revised form 4 June 2019; Accepted 5 June 2019
Available online 18 June 2019

Shock-darkening in ordinary chondrites, as we refer to it in this work, is not the only darkening effect. Partial, or whole-rock melting, and shock veins (both characterized by the presence of micron-sized metal and iron sulfide droplets mixed within the silicate melt) are other mechanisms for darkening ordinary chondrites (Britt and Pieters, 1994; Kring et al., 1996; Sharp et al., 2015; Schmieder et al., 2016). Space weathering, as nanoparticulate iron produced by solar wind irradiation on surface of asteroids, is also a darkening effect (Clark et al., 2002). However, the latter only affects the surface of asteroids (regolith) whereas shock can affect larger volumes of material. Shock-darkening and whole-rock melting in ordinary chondrites strongly affect the reflectance spectra of meteorites (as seen in the Chelyabinsk LL5 chondrite, Kohout et al., 2014 and references therein) by suppressing the 1 and 2 μm silicate absorption bands in spectra. Because classification of asteroids is based on reflectance spectra (DeMeo et al., 2009; DeMeo and Carry, 2014), detection of S-complex asteroids (with spectra showing the 1 and 2 micron silicate absorption bands, and hosting ordinary chondrites) could be more difficult. Indeed, darkened S-complex asteroids will possess spectra similar to those of C-complex asteroids (flat spectra devoid of the 1 and 2 μm silicate absorption bands, DeMeo et al., 2009).

To add to the current study of shock-darkening (spreading of metals and iron sulfides in veins, Kohout et al., 2014, Moreau et al., 2017, 2018), we will link our work to shock metamorphism. In the progressive shock metamorphism of ordinary chondrites, the seven shock stages (C—S1 to C—S7) are based on the modification of the crystal structure of rock-forming minerals: fracturing, lattice deformations and the localized observations of melt pockets and veins. Shock-darkening mostly occurs at conditions characterized by C—S5 and C—S6 (~30–75 GPa), but it can also occur with reduced intensity at C—S3 and C—S4 (~5–30 GPa) (Rubin, 1992; Bennett and McSween, 1996; Rubin et al., 1997; Schmitt, 2000; Wang et al., 2011). The criterion for shock C—S5 (35–45 GPa), as defined by Stöffler et al. (1991, 2018), is the presence of maskelynite glass (Stöffler et al., 1986, Chen and El Goresy, 2000, Stöffler, 2000 and references therein; amorphous plagioclase, Jaret et al., 2015) and strong mosaicism in olivine. C—S6 (55–75 GPa) is marked by the occurrence of plagioclase-composition shock-melted diaplectic glass (Fritz et al., 2017) and abundant melt pockets, veins, or dikes. Whole-rock melt (C—S7) succeeds C—S6 at the ~75–90 GPa transition. Experiments aiming to observe the aftermath of shock compression on fresh samples of meteorites have also been carried out (e.g. Schmitt, 2000; Xie and Chen, 2016) and several studies used shock physics numerical modeling to study effects of shock compression in meteorites (e.g. uncompacted chondrites, Bland et al., 2014, Davison et al., 2016, 2017; thermally metamorphosed ordinary chondrites, Moreau et al., 2017, 2018). Numerical modeling is useful to study high shock pressure effects, because shock experiments are difficult to interpret in terms of melting and post-shock heating, owing to experimental setup limitations (e.g. the reverberation technique subject to superposed shock waves, Langenhorst and Deutsch, 1994; Langenhorst and Hornemann, 2005), and no direct observation of the pressure and temperature distribution after shock is possible at the mm-scale.

As no detailed numerical modeling study exists, illustrating shock effects encompassing C—S5 and C—S6 in ordinary chondrites, we decided to focus on this transition in detail. In a recent systematic study (Moreau et al., 2017), using shock physics numerical modeling in ordinary chondrites, we determined the 40–50 GPa pressure range which is marked by the exclusive melting of iron sulfides. In another study (Moreau et al., 2018), we observed shock wave propagation effects on assemblages of iron sulfides and metals at 45 GPa and concluded that metals are not the main agent of shock-darkening because the melting of metals is only possible in specific configurations of grains in eutectic mixtures. However, in Moreau et al. (2017), we lacked good approximation of silicates, metals and whole sample melting and post-shock heating to study shock metamorphism in more details. Also, in Moreau et al. (2017), our models provided rounded iron and troilite grains in an olivine matrix devoid of open pores; this configuration of grains did not accurately reflect the real petro-fabric of ordinary chondrites.

We aim to build on these partial results and resolve shock compression in ordinary and enstatite chondrites, with higher fidelity. Using realistic numerical samples converted from backscattered electron microscope images (BSE) of meteorite thin sections, we will carry out a systematic study in the 30–70 GPa range. This pressure range is characteristic of the transition from C—S5 and C—S6. The numerical samples include silicates (olivine/pyroxene, plagioclase), metals (iron) and iron sulfides (troilite) using a single approach of eutectic mixtures and open pores. We propose to observe and illustrate:

1. The melting and post-shock heating of individual phases and bulk composition (i.e. modal average of all phases, without the fraction of open pores).
2. The localized effects of pore crushing, and closure of large cracks.
3. The effect of porosity (applied to silicates) on bulk melting and shock-darkening.
4. The effect of pre-heating (Schmitt, 2000) on post-shock heating and melting, during impact events in thermally metamorphosed materials of the parent body.
5. The melting features observed in troilite, olivine and iron.

By default, we limit our models to three mineral phases (i.e. olivine, iron, and troilite) and open pores, thus reducing numerical inaccuracies in shock wave interactions. Hence, we provide only a first-order estimate for the observation of plagioclase melting in a dedicated model. Because of its low abundance in ordinary chondrites (~10 vol%, Hutchison, 2007) plagioclase will contribute only to a small fraction of post-shock heating and melting and does not affect shock-darkening—the metal and iron sulfide darkening veins, although they do not penetrate plagioclase glass, predominantly spread between other silicate cracks (Moreau, 2019). Furthermore, our modeling cannot resolve the occurrence of maskelynite (formation range, 25–40 GPa, anti-correlated to the Ca concentration and dependent on shock duration and phase equilibration; Gibbons and Ahrens, 1977, Stöffler et al., 1991, 2018; Wang and Chen, 2006, Tomioka et al., 2010, Rubin, 2015), whose nature and formation is still not well understood (Chen and El Goresy, 2000; Jaret et al., 2015). However, plagioclase serves as a good marker for the transition from C—S5 to C—S6 in optical microscopy studies.

With these observations, we will illustrate the transition from C—S5 to C—S6 in a novel way. We will compare our results with observations of shock metamorphism, which include shock experiments (e.g. Schmitt, 2000; Kohout et al., 2018). Some of the drawbacks of our approach are the absence of brittle fracturing, lattice deformation, heat transfer, and migration of melt necessary for shock-darkening (Tomkins et al., 2013). We will not include other phases than those mentioned above. Frictional heating (Stöffler et al., 1991; van der Bogert et al., 2003) will not be investigated here (see Section 4.2 in Moreau et al., 2018). Heat diffusion will only be briefly discussed.

## 2. Methods

To study shock-compression of heterogeneous materials including partial melting and post-shock heating associated with shock entropy, shock wave interactions, and the effects of localized heating (hotspots) from pore crushing (Güldemeister et al., 2013), we used the iSALE-2D shock physics code (Wünnemann et al., 2006). The iSALE-2D code is based on the SALE hydrocode solution algorithm (Amsden et al., 1980). To simulate hypervelocity impact processes in solid materials, SALE has been modified to include an elastic-plastic constitutive model, fragmentation models, various equations of state (EoS), and multiple materials (Melosh et al., 1992; Ivanov et al., 1997). More recent improvements include a modified strength model (Collins et al., 2004) and a porosity compaction model (Wünnemann et al., 2006; Collins et al.,

**Table 1**
Mesoscale setup parameters.

| | |
|---|---|
| Width (cells)[a] | 800 |
| Height (cells) | |
| Flyer plate | 800 |
| Buffer plate (top)[b] | 160 |
| Sample plate[c] | 800 |
| Buffer plate (bottom) | 480 |
| Cell size (μm) | 1–2 |
| Boundary conditions | |
| Top, bottom[d] | Outflow |
| Sides | Freeslip |
| Time parameters | |
| Virtual modeling time (sec) | $0.5*10^{-6}$ |
| Modeling step (sec) | $1.5*10^{-10}$ |
| Saved interval step (sec)[e] | $0.2*10^{-8}$ |
| Total saved time steps | 250 |
| Tracer movement algorithm | material |

[a] The general width/height are adapted in one models.
[b] The nominal pressure is recorded from that buffer.
[c] The bitmap files are inserted in that layer and have same size as layer.
[d] The size of the bottom buffer plate ensures the sample does not exit the model.
[e] $0.18*10^{-8}$ and 277 saved steps for A1-albite model.

2011).

The approach we used in this work was similar to that used in previous studies (e.g. Crawford et al., 2003; Ivanov, 2005; Riedel et al., 2008; Borg and Chhabildas, 2011; Güldemeister et al., 2013; Bland et al., 2014; Davison et al., 2016, 2017; Moreau et al., 2017, 2018). In a mm-scale (mesoscale) planar 2-D Eulerian frame of reference (Collins et al., 2012), we generated a planar shock wave by impacting an olivine flyer plate (analogous to shock recovery experiments; e.g. Langenhorst and Deutsch, 1994, Langenhorst and Hornemann, 2005) on top of a series of olivine layers: a buffer plate, a sample plate created from BSE images (see the Supplementary material for details on the conversion), and a secondary buffer plate. Parameters of the optimal mesoscale setup are given in Table 1, for this work. In contrast to Moreau et al. (2018) we did not apply cylindrical symmetry (because of heterogeneous distribution and shape of the phases) to approach a 3-D-like modeling. However, the effects of cylindrical geometry on the post-shock heating and melting have been tested and were minimal for this work (see Supplementary material).

### 2.1. Materials and thin sections

The major components used in the mesoscale models (with all mechanical and thermal parameters adapted from Moreau et al., 2017, 2018) were:

1. Mg-rich olivine (forsterite, using the Analytical Equations of State, ANEOS) as the coarse-grained matrix material. We applied melting temperatures equivalent to the fraction of fayalite (1980–2042 K), or iron content, found in the Mg-rich olivine in ordinary chondrites. We used the same heat capacities integration and heat of fusion (909 kJ $kg^{-1}$) at the melting point for all modeled ordinary chondrite types. For the enstatite chondrite, we used the olivine ANEOS for simulating the Mg-rich pyroxene, enstatite (which possesses the same shock mechanical properties as olivine, Moreau et al., 2017), a 650 kJ $kg^{-1}$ heat of fusion (Hirschmann et al., 1998) and the heat capacities of olivine as they are close to those of enstatite (Krupka et al., 1985). We adapted the lower melting temperature of enstatite (1832 K).
2. Iron (using the ANEOS) to represent the FeNi alloy found in meteorites (1811 K melting point, 292 kJ $kg^{-1}$ heat of fusion).
3. Troilite (using the pyrrhotite-based Tillotson equations of state, Moreau et al., 2017) to represent the iron sulfide phase (1463 K melting point, 368 kJ $kg^{-1}$ heat of fusion).
4. The eutectic mixtures of iron and troilite, if present (Moreau et al., 2018). We distinguished eutectic materials from the main components within Lagrangian tracers (see the Supplementary material for the criteria in detecting eutectics from the BSE images).
5. Empty pores – to this fraction of empty space in the mesh we adapted the silicate porosity to attain the meteorite porosity.
6. Albite to represent plagioclase. Albitic plagioclase in ordinary chondrites is defined as $< An_{20}$ (Van Schmus and Ribbe, 1968; Schmitt, 2000; Kovach and Jones, 2010). We used the albite Tillotson equations of state (Moreau et al., 2018, a 1430 K melting point, and 243 kJ $kg^{-1}$ heat of fusion).

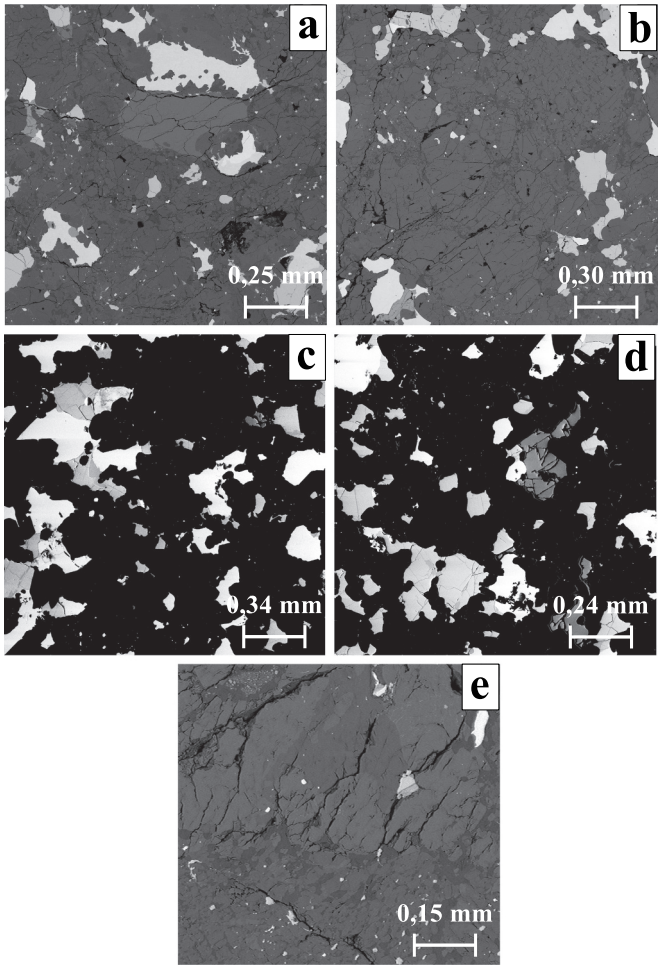


**Fig. 1.** Chosen backscattered electron (BSE) microscope images of Annama H5 (a,b), Neuschwanstein EL6 (c, d), and Chelyabinsk LL5 (e) chondrite thin sections for the modeling. The brightness decreases from metal along troilite, olivine/pyroxene, plagioclase, down to pore space. Images c) and d) resolve only metal, troilite, and enstatite (no cracks/pores implemented in the respective models).

We used the same strength properties as those found in Moreau et al. (2018) for olivine, iron, troilite, and plagioclase with thermal softening. Other specific material modeling parameters, unless specified, are taken from Moreau et al. (2017, 2018).

The BSE images (Fig. 1) we used to characterize the materials represented ordinary and enstatite chondrites. The images were obtained using FEG-SEM Tescan MIRA GMU (CGS, Prague) equipped with Robinson-type BSE detector; the imaging conditions used were following: 15 kV accelerating voltage, 3 nA beam current. Scaling details of images can be found in the Supplementary material. The chosen chondrites were:

**Table 2**
Models and modal distribution of the phases.

| Model | Size (cells) | Scale (μm/cell) | $\%_{Olivine}$[a] | $\Phi_{Olivine}$[b] | $\%_{Pores}$ | $\%_{Iron}$ | $\%_{Iron\text{-}eutectic}$ | $\%_{Troilite}$ | $\%_{Troilite\text{-}eutectic}$ |
|---|---|---|---|---|---|---|---|---|---|
| A1[c] | 800 × 800 | 1.53 | 84.25 | 3.41 | 2.13 | 7.65 | 0.44 | 5.11 | 0.42 |
| A2 | 800 × 800 | 1.89 | 86.16 | 3.33 | 2.13 | 5.21 | 0.39 | 5.72 | 0.39 |
| N1 | 800 × 800 | 1.34 | 79.27 | 3.78 | 0.00 | 12.80 | 1.23 | 5.69 | 1.01 |
| N2 | 800 × 800 | 1.17 | 82.39 | 3.64 | 0.00 | 6.26 | 0.44 | 10.44 | 0.47 |
| C1 | 600 × 562 | 1.00 | 95.11 | 2.86 | 3.28 | 0.50 | 0.12 | 0.88 | 0.12 |
| A1-albite | 800 × 800 | 1.53 | 74.33[d] | 4.08[e] | 1.54 | 7.63 | 0.47 | 5.12 | 0.44 |

[a] The total of all materials may not equal to 100%, values are rounded from the total amount of cells (e.g. 640,000 cells).
[b] Total porosities of the models are given in the text.
[c] This model will also be applied 10% porosity, 15% porosity, and 920 K pre-heating at 10% porosity.
[d] 10.48% of plagioclase in the sample plate.
[e] Same porosity applied in plagioclase.

1. Annama H5 ordinary chondrite, 8% porosity (Kohout et al., 2017), $Fo_{81.4}$ olivine composition, 2 models (A1 and A2, from Fig. 1a/b).
2. Neuschwanstein EL6 enstatite chondrite (Russell et al., 2003), ~4% porosity (Kohout et al., 2010) dominated by enstatite silicate and high abundance of FeNi metals and iron sulfides, 2 models (N1 and N2, from Fig. 1c/d). The melting temperature of the eutectic mixtures was taken directly from Mare et al. (2014) without consideration of the Ni content of metals. The generated sample plates did not display open pores due to the low total porosity of the meteorite and under-resolved porosity in the BSE images.
3. Chelyabinsk LL5 ordinary chondrite (Kohout et al., 2014), 6% porosity, $Fo_{72}$ olivine composition, one model (C1, from Fig. 1e). The porosity is well resolved in the BSE image and it offers an opportunity to observe more post-shock heating effects from crack closure. It is worth noticing that some cracks in the BSE images may result from sample preparation. The chosen BSE image is that of a light-colored lithology clast of the Chelyabinsk meteorite (Kohout et al., 2014).

We have compiled the characteristics of the converted images to sample plates in Table 2, showing the model names, mesh parametrizations, and fractions of materials. In the BSE images, we ignored other phases such as chromite, phosphate and other phases that we converted to the principal phases. Because a single thin section does not represent the exact modal composition of a meteorite, these simplifications were trivial. We applied an initial porosity of 5%, rather than 8%, in the A1 and A2 models, because in A1, the porosity is enhanced to 10% and 15% to complete a systematic porosity study. We also applied a 3% total porosity in the N1 and N2 models, consistent with the average porosity of enstatite chondrite falls (Macke et al., 2010).

### 2.2. Post-shock temperatures and melting

In Moreau et al. (2018) we detailed the method to assess the post-shock temperature and melt fraction α of a given phase. We briefly describe the method here.

For assessing melting, we used peak shock pressures recorded in tracers (Wünnemann et al., 2008; Moreau et al., 2017, 2018); we paid attention to account for reflections by taking the mean of all peak shock pressures recorded by tracers through the modeling time (reverberation effect). Post-shock temperatures and melt fractions were assessed from the combination of heat capacity integration, within the range of temperatures to the melting point, heat of fusion, and the total shock and release specific energy at a given peak shock pressure (Moreau et al., 2017, 2018). Absolute values of post-shock temperatures are used to quantify post-shock heating.

In the presence of an iron-troilite eutectic mixture, we used simplified thermal properties with melting temperature and heat of fusion assigned to each ordinary chondrite type based on its nickel content (high to low Ni contents, LL-H, 1201–1256 K, 270–294 kJ $kg^{-1}$, Mare et al., 2014, Tomkins, 2009). The melting temperature of the eutectic mixtures varies according to the Fe/S ratio. However, because of the highly heterogeneous distribution of post-shock temperatures (Moreau et al., 2017, 2018) and the absence of heat diffusion (important in melting metals and iron sulfides, Tomkins, 2009, Tomkins et al., 2013), we considered the eutectic equivalent to 31.6 Wt% S (Mare et al., 2014), applying the same individual melting temperature to iron and troilite in the mixtures.

To categorize our results, we used the nominal pressure as a marker. The nominal pressure is the pressure recorded in the pure olivine buffer above the sample and allows us to compare our results with the shock classification based on the pressure in pure olivine (Stöffler et al., 1991, 2018).

### 2.3. Porosity

In each model we applied the porosity by considering two parts. First, we introduced the resolved porosity from BSE images as resolved pores in the mesh. Secondly, we distributed any additional remaining unresolved porosity up to the total value of the model porosity in the olivine/enstatite, using the ε–α compaction model (Wünnemann et al., 2006; Collins et al., 2011); all parameters can be found in Moreau et al. (2017, 2018). If plagioclase is present in the model, the porosity is applied to both olivine and plagioclase. In this work, the additional heating of the plastic work due to pore crushing is omitted from the post-shock temperature assessment – but not from the peak temperatures recorded by iSALE. We give more insight on melting at the peak of the shock (peak temperatures) in the Supplementary material.

### 2.4. Resolution

Because grains in the meshes varied as a function of the number of constitutive cells, we carried out resolution tests on rounded grains from 3 to 126 cells per grain radius (CPGR) with a fixed cell size of 1 μm. Results for the peak shock pressures and melt fractions are shown in Fig. 2 at a nominal pressure of 45 GPa. The 3 CPGR grain only showed a difference of 10% in pressures (and post-shock temperatures) compared to the 126 CPGR grain. The melt fraction seemed to depend more on the resolution because grains with more constitutive cells better displayed very localized heating and shock wave effects (Moreau et al., 2018). These variations were independent of the chosen cell size; the values of the 96 CPGR grain for 1, 1.5, and 2 μm cells did not show large variations (< ~0.01% in pressure and temperature; < 10% in melt fraction in the very localized melt zone which contributed only to ~3% of the grains). Because there were only a small number of grains with ≤6 CPGR (e.g., in one chosen thin section, < 0.6% of troilite grains ≤6 CPGR were present in the whole sample plate), we considered the relative errors of the final results to be minimal and disregarded the presence of under-resolved grains.

To test further this approach of resolution, we removed all ≤6

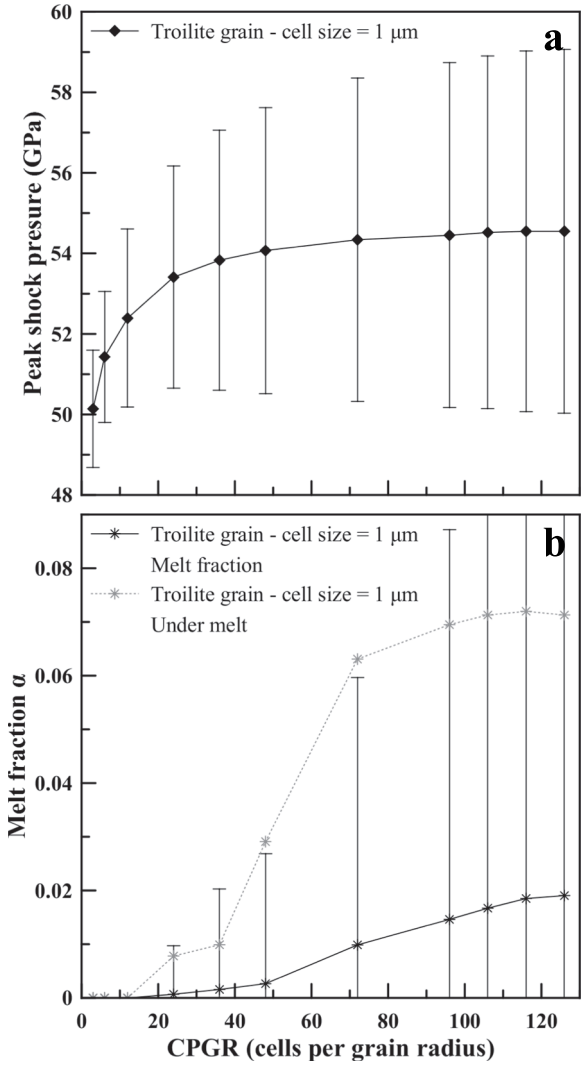


**Fig. 2.** Resolution tests on rounded particles at different cells per grain radius CPGR numbers (fixed cell size of 1 µm) with a) average peak shock pressures and b) melt fractions α. The grain sizes vary from 6 to 252 µm in diameter. The tests showed equivalent results (with minimal errors) using cell sizes of 1.5 or 2 µm.

CPRG grains in one model and the results only varied by < 1%. We also tried to smooth the grain edges, using ellipsoidal grains, and obtained very similar results to the original model (see Supplementary material). We, thus, accept that the resolution present in our work does not impair the general results, which will depend mostly on bigger and better resolved grains. This applies also for the pores. In the model including plagioclase, we deleted very irregular plagioclase grains when they had very few cells, as treating > 2 or 3 phases is usually not recommended in mesoscale modeling.

## 3. Results

For each model, we ran a series of 10 simulations at nominal pressures between 40 and 70 GPa. We carried out four more series of models using model A1 with 10% porosity, 15% porosity, and initial temperature of 920 K with 10% porosity (consistent with Schmitt, 2000 and the 9% porosity Kernouvé meteorite and 920 K pre-heating). Also, we simulated a model similar to A1, labeled A1-albite, including the plagioclase phase, albite (Table 2), and starting the systematic study at 30 GPa. All models, and A1 porosity/pre-heating variants, display different sets of nominal pressures due to the ε–α compaction model and thermal softening in olivine in the layers.

We provide a series of figures and tables compiling the main results:

1. In Figs. 3, 4, 5 and 6, we provide mapping for the materials, peak shock pressures, post-shock temperatures, and melt fractions at ~55 GPa nominal pressure (~50 GPa for Fig. 6) of A1 and A2, N1 and N2, C1, and A1-albite, respectively. Snapshots of post-shock temperatures and melt fractions are arbitrarily shown right after compression. Several areas of interest are annotated for further discussion.
2. The detailed results from all models are compiled in separate tables in the Supplementary material document (Tables A1–A9). The tables list the following values for the individual materials and the bulk: nominal pressure ($P_N$, GPa), peak shock pressure ($P$, GPa), post-shock temperature ($T$, K), amount of material that started to melt ($m$, %), and melt fraction α. Some values are given standard deviations to provide a measure of the heterogeneity of the results. All results presented in this work are given for the original area of tracers (mass weighted averages), excluding the pore fraction and the compressive state shown in some figures.
3. For all models, in Fig. 7, we compile melt fractions of the individual phases and bulk (Fig. 7a–d), and bulk peak shock pressures and post shock temperatures (Fig. 7e/f) as a function of the nominal pressure. In Fig. 8 we differentiate eutectic and non-eutectic melting for troilite and iron in models A1 and N1.

### 3.1. Post-shock heating and melting

Each phase (except for the pre-heated and porosity enhanced models A1, and A1-albite) shows the following:

1. Troilite started to melt below 40 GPa of nominal pressure (Fig. 7a) and below 68 GPa the melt fractions α progressively reached values between 0.7 and 0.9. The Neuchwanstein models N1 and N2 displayed the highest variation in troilite melting (Fig. 7a). This can be explained by the fact that the troilite is not homogeneously distributed in the Neuschwanstein models resulting in a factor of two difference in troilite abundance between the two models. In eutectic melting (Fig. 8a), troilite started to melt below 40 GPa with a higher observed melt fraction α compared to the non-eutectic phase, because of lower melting temperatures. At the highest nominal pressure of ~68 GPa, the recorded averaged post-shock temperatures in troilite were lowest in C1 (1555 K) and highest in N1 (1775 K).
2. Iron showed effective melting only from 50 GPa (Fig. 7b), with the strongest excursions to higher melt values in N1 and C1. However, the melting was mostly related to the eutectic iron (see Fig. 8b) due to the lower melting temperature of the eutectic. In any case, the iron melt fraction α remained very low compared to troilite. At the highest nominal pressure of ~68 GPa, the recorded averaged post-shock temperatures in iron were lowest in C1 (1090 K) and highest in A2 (1140 K).
3. Olivine (enstatite in N1 and N2) started to melt at ~50 GPa with low values of melt fraction α equivalent to iron values (Fig. 7c)—this is dependent on the fraction of iron material. The most efficient melting of enstatite in N1 is not only explained by the lower melting temperature of enstatite but also by external factors that will be discussed below—no specific excursion of melting was observed in N2 for enstatite. At the highest nominal pressure of ~68 GPa, the recorded averaged post-shock temperatures in olivine (enstatite) were lowest in C1 (1080 K) and highest in N1 (1303 K).
4. Melting of the bulk was progressive (Fig. 7d) from 40 GPa up, but very dependent on the individual phases (mostly troilite). The melt fraction reached a maximum value of 0.09 in N1 with 13.2% of the material at the melting point at 68 GPa nominal pressure. In the 40–70 GPa range, recorded bulk post-shock temperatures ranged from ~600–700 K to ~1100–1300 K.

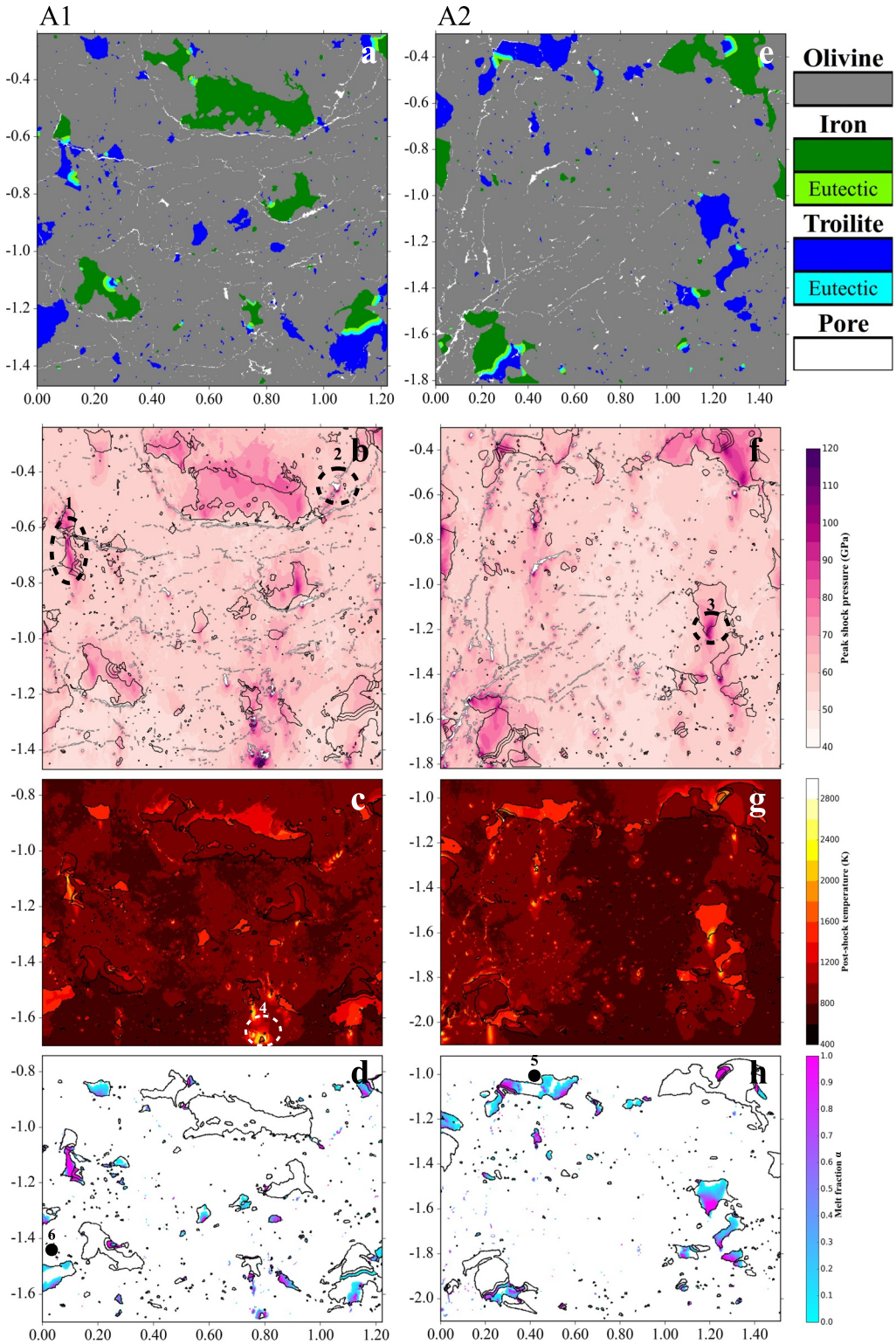


**Fig. 3.** Model snapshots from A1 and A2 shocked at 55 GPa nominal pressure, depicting the sample plates (a, e), the recorded peak shock pressures (b, f), the post-shock temperatures (c, g) and the melt fractions α (d, h). The sample plate and peak shock pressure panels are shown in an uncompressed state. The other panels are shown in a compressed state right before release. Annotations above dashed circles or dots show areas of interest. The graduations are in millimeters.

### 3.2. Porosity effect

Differences in the above-mentioned trends were observed in A1, with enhanced porosities of 10% and 15% for olivine. Heating and melting of olivine increased with porosity at same (nominal) pressures. We observed the same trend, to a lower degree, with iron and troilite due to changes of impedance with the more porous olivine. At ~67 GPa, the olivine melt fraction varied from 0.01 at 5% porosity to 0.12 at 15% porosity, and the bulk melt fraction and post-shock temperature values shifted accordingly from 0.05 and 1168 K at 5% porosity to 0.15 and 1860 K at 15% porosity.

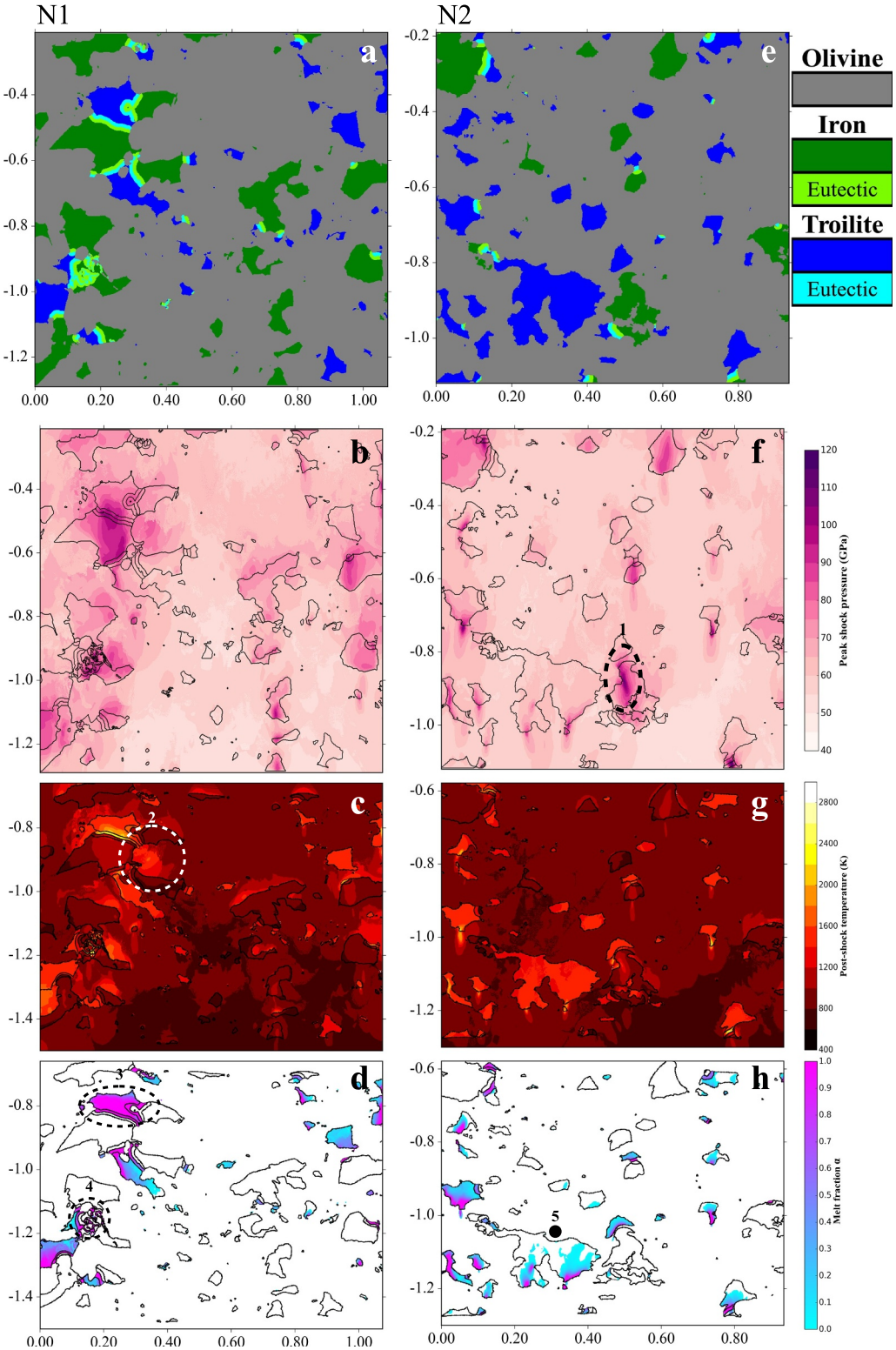


**Fig. 4.** Model snapshots from N1 and N2 shocked at 54 GPa nominal pressure, depicting the sample plates (a, e), the recorded peak shock pressures (b, f), the post-shock temperatures (c, g) and the melt fractions α (d, h). Melting temperature of enstatite was used for these models.

### 3.3. Pre-heating effect

In the 920 K pre-heated model A1 at 10% porosity, melting for all phases occurred at lower pressures (see Fig. 9). Comparing with A1 at 10% porosity, the results are:

1. iron started to melt at pressures ~15 GPa lower than those in the non pre-heated model. At ~66 GPa, the non-eutectic iron melt fraction reached a value of 0.019 in the pre-heated model.
2. troilite started to melt at 38 GPa with a melt fraction of 0.27, and complete melting was achieved starting at 53 GPa (melt fraction: 1) in the pre-heated model; in the original model, troilite only reached

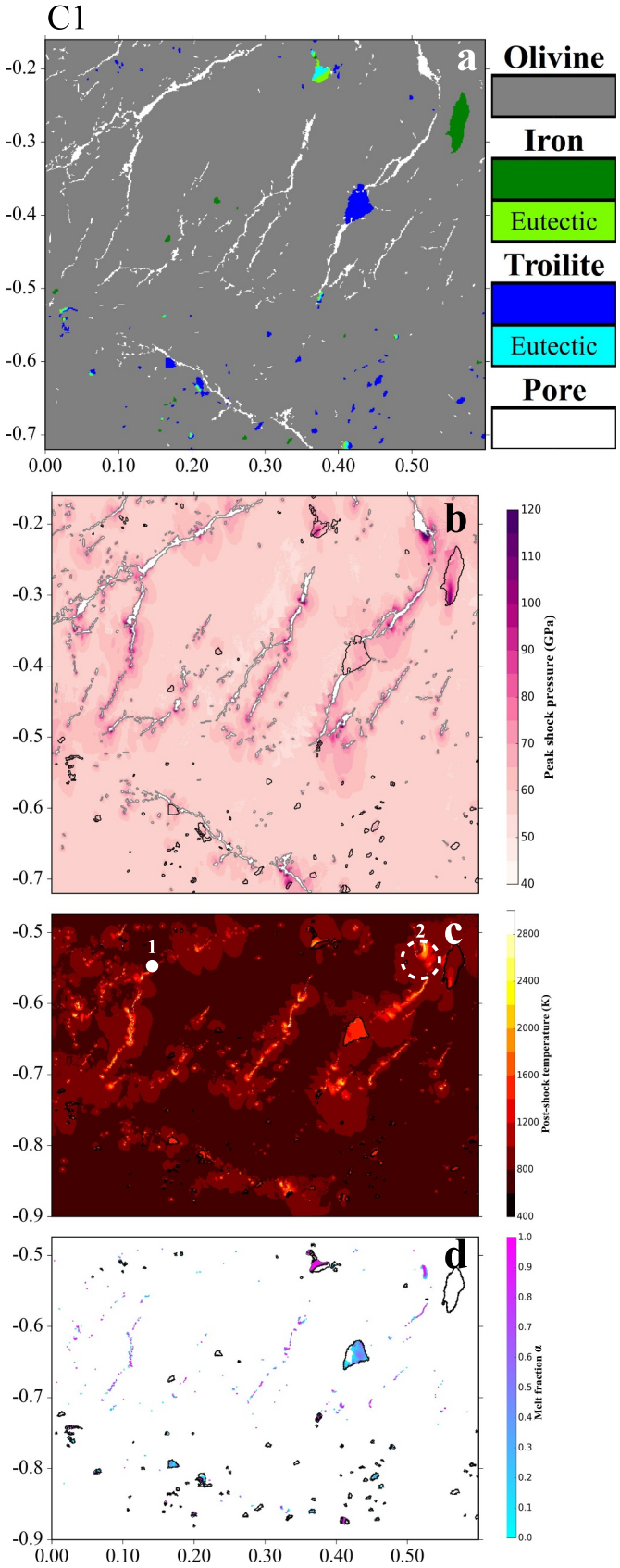


**Fig. 5.** Model snapshots from C1 shocked at 55 GPa nominal pressure, depicting the sample plate (a), the recorded peak shock pressures (b), the post-shock temperatures (c) and the melt fractions α (d).

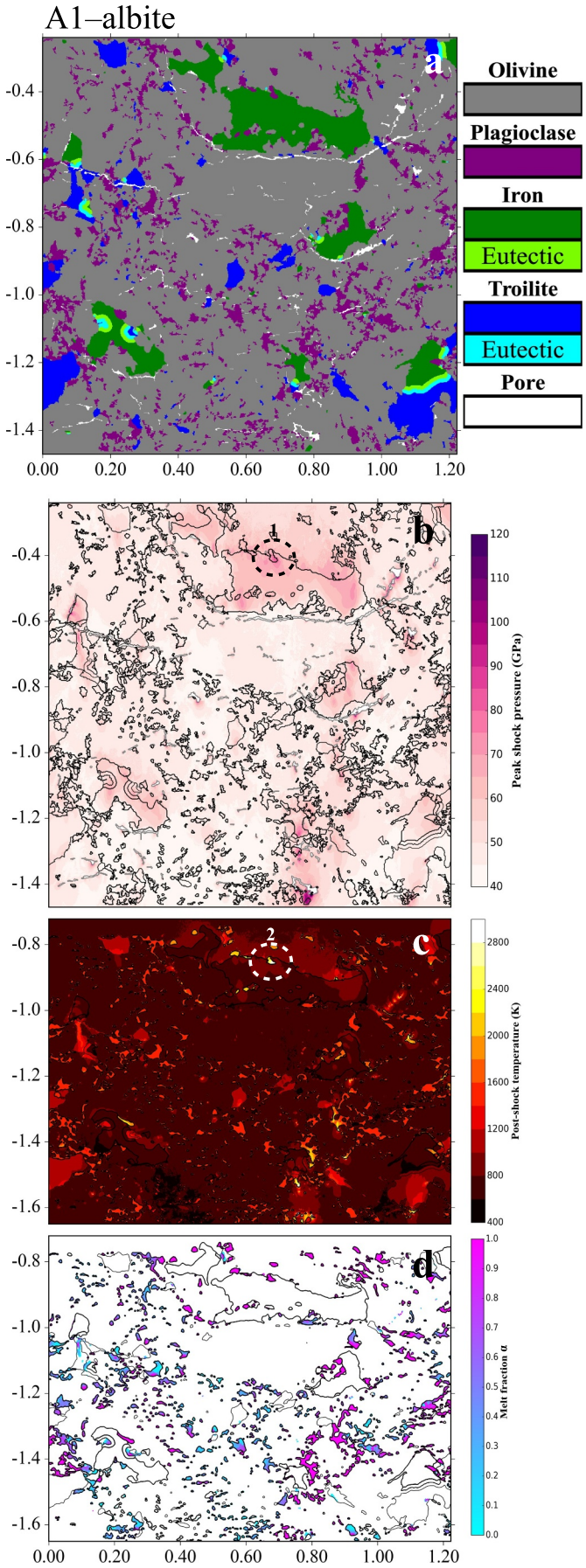


**Fig. 6.** Model snapshots from A1-albite shocked at 49 GPa nominal pressure, depicting the sample plate (a), the recorded peak shock pressures (b), the post-shock temperatures (c) and the melt fractions α (d).

a melt fraction of 0.79 at ~67 GPa.

3. at ~66 GPa in the pre-heated model, the melt fraction of olivine shifted from a value of 0.03 in the original model to 0.11 in the pre-heated model.
4. pre-heating the model doubled the melt fraction for the bulk at ~66 GPa, from 0.07 to 0.15, with an increase of ~500 K in post-shock temperatures. The computed difference in post-shock temperatures (~500 K) is smaller than the rise in temperature, 293 K to 920 K (> 600 K), from pre-heating the model. This difference is explained by the integration of heat capacities taken from 920 K, and not 293 K, and the related shock entropy (see Moreau et al., 2018 and references therein). Peak shock pressures are little affected in the pre-heated model compared to the original model.

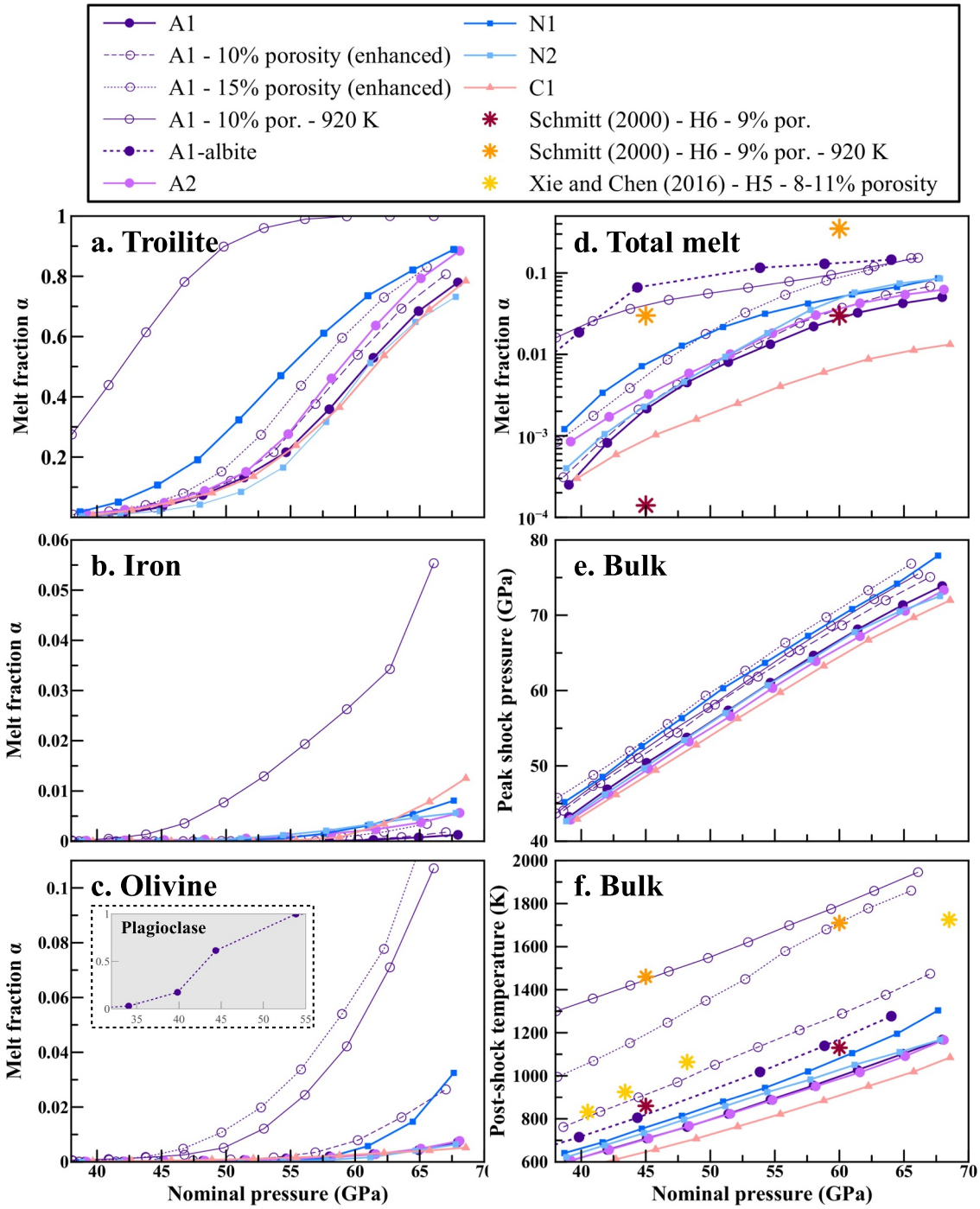


**Fig. 7.** Melt fractions α for: a) troilite, b) iron, c) olivine and plagioclase, and d) the bulk composition; peak shock pressures and post-shock temperatures of e,f) the bulk composition—for all models at the 40–70 GPa nominal pressure range. The stars are values from Schmitt (2000), which represent: the percentage of molten areas identified in a shocked sample (Kernouve H6 chondrite) for any melt containing a mixture of metals, iron sulfides, and silicates, and related post-shock temperatures; and values from Xie and Chen (2016). For Xie and Chen (2016) data, the nominal pressures we used are the initial pressures in their shock-recovery experiments. Graphic d) has a logarithm scale. The results for model A1-albite are displayed only in graphics c), insert, d), and f), because the model values overlap with model A1 in some graphics.

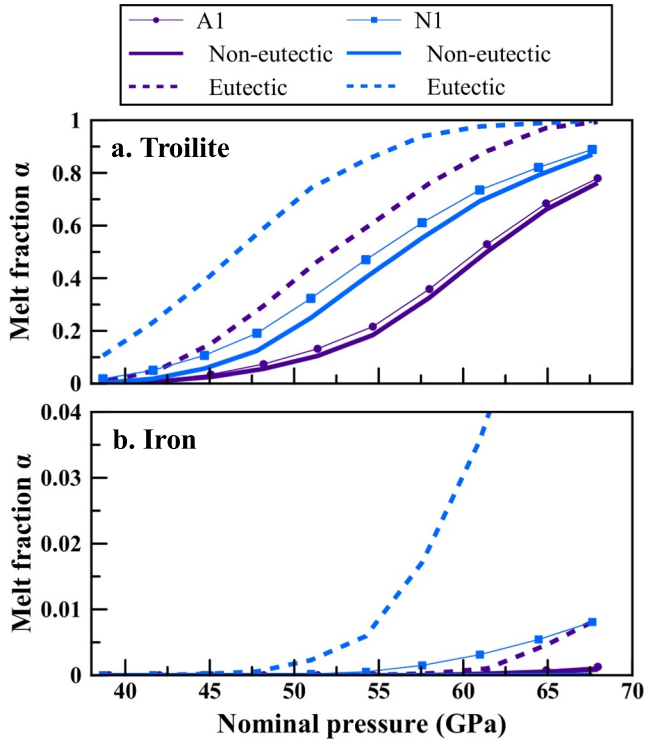


**Fig. 8.** Eutectic and non-eutectic melt fractions α for: a) troilite and b) iron, from A1 and N1 models at the 40–70 GPa nominal pressure range. The plain marker lines are the combined results for the non-eutectic and eutectic materials (as seen in Fig. 7).

### 3.4. Plagioclase

Finally, there are the following differences in the results of the Annama model that included plagioclase (A1-albite). The bulk post-shock temperatures are higher for A1-albite due to the very high post-shock temperatures recorded in plagioclase (from ~1000 K at ~30 GPa nominal pressure to ~2500 K at ~64 GPa). Thus, with the fraction of plagioclase present in the model, at ~63–64 GPa, the post-shock temperature is > 200 K higher than in A1. Plagioclase starts to melt, prior to other phases, at ~30 GPa with a 0.01 melt fraction and complete melting at ~54 GPa with a 1.00 melt fraction. This affects the general results when estimating the melt fraction for the bulk (see Fig. 7d).

## 4. Discussion

The observed post-shock heating and melting of the phases and the bulk composition from our models are in good agreement with what is observed in shock metamorphism of ordinary chondrites (Stöffler et al., 1991, 2018; Bennett and McSween, 1996, Rubin et al., 1997. Schmitt, 2000, Xie and Chen, 2016, Bischoff et al., 2018). The studied pressures in this work are related to C–S5 and C–S6 in the 30–70 GPa range, below the limit to the whole-rock melting at C–S7 (Stöffler et al., 1991, 2018; Fritz et al., 2017). In our work, the dominant melting of troilite and plagioclase over the other phases is characteristic of the C–S5 to C–S6 transition. The melt fractions of olivine and iron (representing the FeNi metal alloy) at 50 GPa are low and slowly increase with increasing pressures. The melting of olivine or iron (if diffusion of heat leads to iron melting) is localized at the iron boundaries, the rear of iron and troilite grains, or in the vicinity of crushed pores. The localized melting is consistent with the melt pockets of silicates and metals observed at C–S5 and C–S6 (Stöffler et al., 1991, 2018; Bennett and McSween, 1996; Rubin et al., 1997; Schmitt, 2000), and also with the intermixed melting of plagioclase and metals often observed in ordinary chondrites at low shock stages (Fig. 3B in Tomkins, 2009; Fig. 2 in Tomkins et al., 2013).

### 4.1. Troilite and iron

Melting of troilite is localized in the bottom of grains (relative to the shock direction, Fig. 3, annot. 3), border (Fig. 3, annot. 5, 6, Fig. 4, annot. 5), and in the case of small grains melting occurs in the whole grain area. This is consistent with the results for simplified grain shapes studied in Moreau et al. (2018). These features are similar to petrographic observations of shocked meteorites from Bennett and McSween (1996). They observed that in an L chondrite shocked at ~50 GPa the most common type of melting generates small droplets (e.g. 10–20 μm) of troilite and causes the melting of troilite on the borders of larger grains. The melting of troilite is also influenced by iron, such as in N1, Fig. 4 (annot. 3), and the grain geometry (Fig. 3 annot. 1). In Fig. 10 we compile melt fractions in troilite as a function of the grain area at two chosen nominal pressures in A1. At any pressure, we observe a group of small grains with higher melt fractions than bigger grains. However, because melting is independent of the grain size (see Resolution section), our observations and those of Bennett and McSween (1996) are a function of the grain shape only, rather than grain area.

The quasi absence of iron melting, with pure iron shock-melting happening at > 120 GPa (see also Ahrens et al., 1998), is consistent with the very rare metal melt droplets identified in Bennett and McSween (1996) at C–S4 and C–S5 in eutectic mixtures or mixed melt pockets (Stöffler et al., 1991, 2018). In our work, the melting of iron is mostly a consequence of eutectic melting (Fig. 4 annot. 4, Fig. 8b) or localized pressure effects due to the grain shape (Fig. 4 annot. 1). Although heat diffusion is not included in our models, iron is often in proximity to hotspots such as those from crushed pores (Fig. 3 annot. 4), heated silicates (e.g. plagioclase) or troilite (Fig. 4 annot. 3). Such temperature gradients may lead to the diffusion of heat into the colder iron. Preliminary results, using a 2-D heat diffusion code in model outputs from Moreau et al. (2018), showed that melting of iron can, indeed, be triggered by heat diffusion in contact with troilite grains (Moreau and Schwinger, 2019).

### 4.2. Olivine and enstatite

The melting of olivine, or enstatite in models N1 and N2, is observed in all models. In addition to the pressure effects studied in Moreau et al. (2017, 2018) (Fig. 3, annot. 3; Fig. 4 annot. 2), we emphasize the melting related to localized heating by the crushing of open pores (Fig. 3 annot. 2, 4; Fig. 5 annot. 1, 2; also illustrated in Fig. 9).

Shock melting of pure olivine occurs only at pressures > 100 GPa. Because whole-rock melting occurs at pressures starting from 75 to 90 GPa at C–S7 (Stöffler et al., 1991, 2018; Fritz et al., 2017), it combines localized melting (pores) and entropy melting of high melting-point silicates (e.g. enstatite or olivine) due to heterogeneities in the peak shock pressures and post-shock temperatures. The transition to C–S7 is also dependent on the precursor material porosity, this is illustrated in A1 at 10% and 15% porosity. As an example, in the model at 15% porosity, the same bulk melt fraction of 0.05 is attained ~10 GPa prior to the 5% porosity model, and the bulk melt fraction reached a value of 0.15 at 66 GPa, about three times higher than the model at 5% porosity and same pressure. The recorded post-shock temperatures in olivine in A1 at 15% porosity are so high (~1920 K) at the highest nominal pressure that, in the vicinity of hotspots, phases will possibly melt by heat diffusion and generate more melting. The pre-heating conditions in thermally affected asteroids, thus attaining whole-rock melt (C–S7) at lower pressures, are well illustrated by the pre-heated model A1 (Fig. 9), meaning that C–S7 will be attained at much lower pressures than in the classification (approx. 10–15 GPa below published values, see Results, and correlating well with results from Schmitt, 2000 re-used in the new classification scheme by Stöffler et al., 2018).

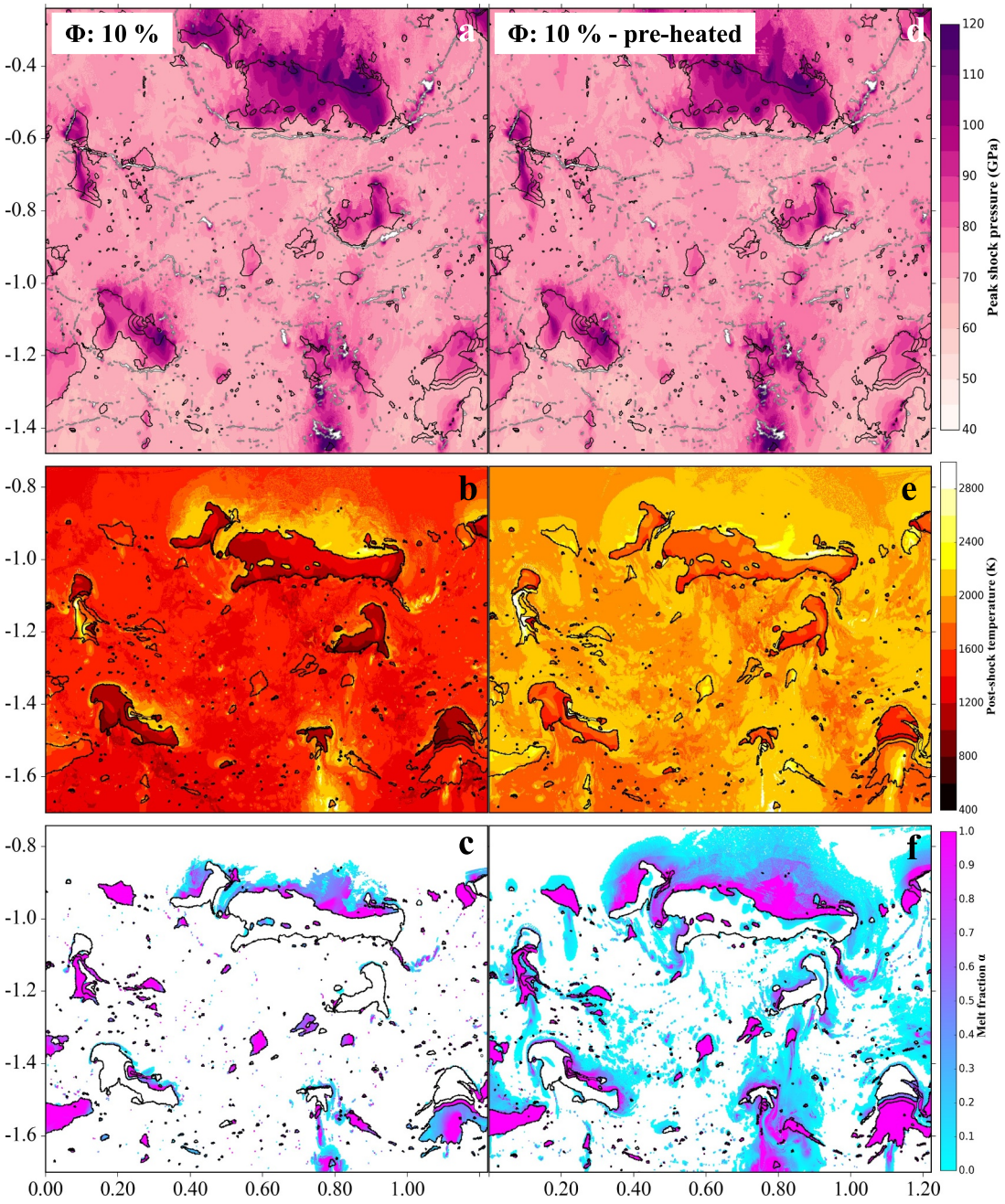


**Fig. 9.** Model snapshots from a–c) A1 at 10% porosity (Φ) and d–f) A1 at 10% porosity, 920 K pre-heating, both shocked at ~66 GPa of nominal pressure. The recorded peak shock pressures (a, d), the post-shock temperatures (b, e) and the melt fractions α (c, f) are shown, respectively. The peak shock pressure panels are shown in an uncompressed state. The other panels are shown in a compressed state right before release. The graduations are in millimeters.

### 4.3. Plagioclase

Our results show that plagioclase is a phase that melts prior to other silicates, metals and iron sulfides. Plagioclase heats easily and may contribute to the melting of nearby phases by heat diffusion if temperatures are high enough. To illustrate this phenomenon, when plagioclase is in contact to iron and is strongly heated by pressure reflections (Fig. 6 annot. 1, 2), the heat diffusion may play an important role in heating and melting iron (a possible explanation for the melting features observed by Tomkins, 2009, Fig. 3B, or Tomkins et al., 2013, Fig. 2). In general, between nominal pressures of 35–40 GPa, post-shock temperatures in plagioclase exceed the melting temperature of the eutectic (metals and iron sulfides), and at 54 GPa nominal pressure, they exceed the melting temperature of olivine. Melting of plagioclase is first dominant at the bottom of the grains, as observed in troilite. The observation of complete plagioclase melting is consistent with the shock classification of Stöffler et al. (1991, 2018). In Ostertag (1983), plagioclase melt glass from shock experiments is only observed above 45 GPa regardless of the plagioclase composition and this is consistent with our observation of partial to complete melting of plagioclase from 45 GPa to 55 GPa.

### 4.4. Bulk post-shock heating and melting

The bulk post-shock temperatures are averaged by the individual phases and the modal composition. In N1, at 68 GPa nominal pressure, post-shock temperatures are 1318 K in olivine, 1089 K in iron and 1786 K in troilite with bulk post-shock temperatures of 1317 K. In all

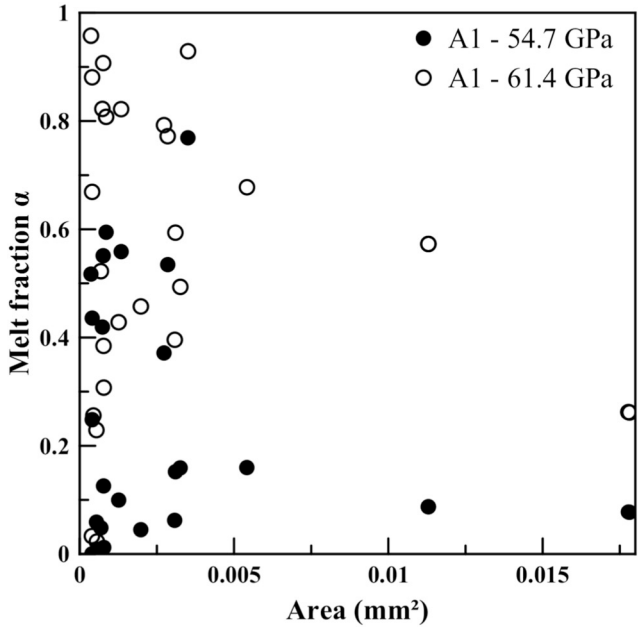


**Fig. 10.** Melt fractions α in function of the troilite grain areas at two chosen nominal pressures. The chosen grains for this graphic all have a minimum number of constitutive cells of 144. The grains do not include eutectic contacts and areas are given for the uncompressed material.

models, the high temperatures in troilite are balanced by more abundant colder iron which equilibrates the bulk post-shock temperature to that of olivine. Bulk post-shock temperatures are, however, very dependent on the iron content, which reflects shock waves and rises the pressures and temperatures in the vicinity (Schmitt, 2000; Moreau et al., 2017), or plagioclase content (model A1-albite), which displays very high post-shock temperatures. Bulk post-shock temperatures could also represent the equilibrium after diffusion of heat between the cold and hot phases (heating of iron and cooling of troilite in contact, Moreau and Schwinger, 2019), but also the generated hotspots from pore crushing.

The post-shock temperatures from our models are similar to those from shock experiments (Fig. 7f; Schmitt, 2000, Xie and Chen, 2016), and theoretical Hugoniot data calculations (Schmitt et al., 1994). The shock experiments carried out on the Kernouvé H6 chondrite (10 vol% in metals, 9% porosity) by Schmitt (2000) displayed post-shock temperatures (computed from the Hugoniot data) between our results for A1 at 5% and 10% porosity. In addition, the pre-heated A1 model at 10% porosity shows very similar post-shock temperatures to the pre-heated shocked samples in Schmitt (2000). Experiments on the Jilin H5 ordinary chondrite (Xie and Chen, 2016; 8–11% porosity, Li et al., 2012) produced slightly higher post-shock temperatures than our results and those of Schmitt (2000). This is either a consequence of iron content, the precursor porosity of the samples (not mentioned in Xie and Chen, 2016), or the effect of post-shock temperatures originating from superposed pressures (Langenhorst and Deutsch, 1994; Langenhorst and Hornemann, 2005) as the peak pressures in Xie and Chen (2016) are twice as high as the initial pressures.

The melting in terms of percent of area estimated by Schmitt (2000) is difficult to compare with our observations at 45 GPa, but correlates well at 60 GPa, for all 3–10% porosity models at room temperature. In pre-heated conditions, the melting results of Schmitt (2000) and A1 pre-heated model are similar at 45 GPa, but our results are a fourth of Schmitt's (2000) results at 60 GPa. Such differences can be explained by the absence of heat diffusion in the simulations (see contrasts of temperatures in Figs. 3–6, 9), the absence of plagioclase in the pre-heated A1 model (plagioclase contributes to 10% of melting already > 55 GPa in A1-albite model), but also it depends on the effects of recrystallization, the conditions of the shock-recovery experiments and other effects that are not reproduced in our models (see Introduction).

Between 45 and 60 GPa, the post-shock temperatures in our models range between ~700 and ~1300 K for all 3–10% porosity models including A1-albite, at 293 K initial temperature. This is in good correlation with the limit range of pressures and post-shock temperatures between C–S5 and C–S6 (45–60 GPa, 900–1100 K, 600–850 °C, Stöffler et al., 1991) in the shock metamorphism of ordinary/enstatite chondrites (Stöffler et al., 1991, 2018; Fritz et al., 2017). In general, most values of post-shock temperatures and bulk melting of individual phases or the bulk composition are correlated to the amount of iron (i.e. metals) in the meteorite, or anti-correlated to the oxidation state from reduced EL and H chondrite models (N1, N2, A1, A2) to the more oxidized LL chondrite model (C1).

### 4.5. Closure of cracks

The effect of crack closure on localized heating/melting of surrounding material is well illustrated in the Chelyabinsk model C1. We observed that the orientation of the cracks influences the heating and melting of the surrounding material (Fig. 5 annot. 1). Cracks oriented at a low angle relative to the shock wave front generate less heating than those oriented at a higher angle. To confirm this observation we provide results from models in which we resolved a single elongated pore (~20 × 200 cells, corresponding to an area of ~0.004 mm$^2$) oriented to the shock wave front at angles from 0° (parallel) to 90° (perpendicular). In Fig. 11 (and numerical results in Table A10) we show the results for the melt fraction α and post-shock temperatures in the olivine material in the sample plate (400 × 420 cells, original area: 0.168 mm$^2$). We observe that the melt production is more important with cracks oriented between 60° and 90°; post-shock temperatures peak with cracks oriented between 45° and 60° relative to the shock wave front.

### 4.6. Shock-darkening

We observed that troilite melting dominates the 40–60 GPa pressure range at 3–15% porosity over olivine and iron; this supports the excess melting of iron sulfides over metals in shock-darkening (Stöffler et al., 1991; Rubin, 1992). This range is also wider than in our previous work (Moreau et al., 2017) because the melting of olivine in the cited work was overestimated. Olivine melting is seldom observed in shock-darkening.

Shock-darkening happens at a wide range of pressures (i.e. shock stages; Rubin, 1992, Bennett and McSween, 1996, Rubin et al., 1997, Wang et al., 2011). Here, we compare observations that support the 40–60 GPa range (C–S5 and C–S6) for shock-darkening:

1. In Bennett and McSween (1996), the only shock-darkened features were observed in the McKinney L4 meteorite classified as C–S6. In Rubin et al. (1997), shock-darkening in enstatite chondrites was most observable in a C–S5 meteorite. In Rubin (1992), who provides more insight into shock-darkening, the observation of shock-darkening is greatest for C–S4 to C–S6 meteorites. It is mentioned here that shock-darkening is effective within eutectic mixtures, explaining the shock-darkening at lower shock stages. In Wang et al. (2011), within their observations on 47 H-chondrites between C–S1 and C–S5, only 4 displayed shock-darkening features: 1 at C–S2, 1 at C–S3 and 2 at C–S4; there was only one C–S5 classified meteorite in their observations.
2. In Schmitt (2000), the metal and/or iron sulfide injections or opaque shock veins are observed from 30 GPa up to 60 GPa, relating lower pressure observations to eutectic melting. Additionally, in Schmitt (2000), small but clear patches of shock-darkening are observed (Moreau, 2019) for a sample experimentally shocked at 60 GPa from steel, amounting to ~40 GPa of shock entropy in the sample due to the effect of the reverberation technique used in the

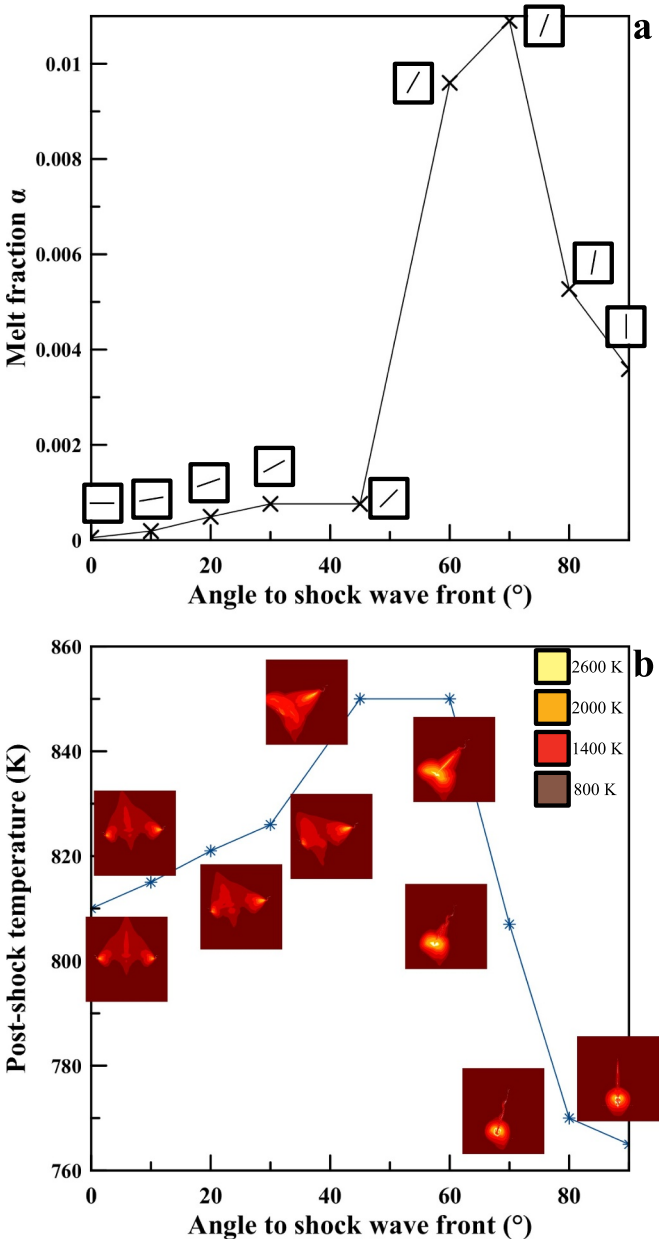


**Fig. 11.** a) Melt fractions α and b) post-shock temperatures from 400 × 420 cells olivine sample plate models used to study the orientation of an open crack (20 × 200 cells) to a shock wave front. Snapshots in a) show the original positions of the cracks (angle) in the sample plate and b) the distributions of the post-shock temperatures after closure of the cracks. The nominal pressure is 63 GPa.

experiment (Schmitt, 1995; Langenhorst and Deutsch, 1994; Langenhorst and Hornemann, 2005; Moreau, 2019). With a similar shock-recovery experiment, as stated above, a light-colored lithology of the Chelyabinsk LL5 chondrite shocked at ~39 GPa did not display shock-darkening (Moreau, 2019). These two observations support the lower range for sock-darkening (40 GPa).

3. Furthermore, a spherical shock-recovery experiment on a 13% porous ordinary chondrite (Saratov L4, Bezaeva et al., 2010) produced very few zones of shock-darkening in a zone shocked at ~40 GPa initial shock pressure (~70–80 GPa at peak pressure), accounting for a total shock pressure between 40 and 70 GPa. Shock-darkening also occurred, as a sharp dark ring, in another spherical shock-recovery experiment on the light-colored lithology of the Chelyabinsk LL5 chondrite, at pressure ~50 GPa (Kohout et al., 2018; Petrova et al., 2018). These observations favor our own estimations of the shock-darkening range (40–60 GPa) and the C–S5 and C–S6 transition scheme.

In general, shock-darkening is difficult to observe in naturally shocked ordinary chondrites considering the narrow pressure range for shock-darkening and that ordinary chondrites classified as C–S5 and C–S6 are not abundant (except for L chondrites, Bischoff et al., 2018). It is also demonstrated that volumes of material shocked above 40 GPa in collisions between asteroids do not exceed half of the projectile volume with impact velocities below 7 km/s (Moreau, 2019), which may explain the very few observations of C–S5 and C–S6 in ordinary chondrites (Bischoff et al., 2018). Under hot conditions (e.g. radiogenic heating; thermal metamorphism, Norton, 2002), shock-darkening can happen at lower pressures, as demonstrated by the pre-heated model in our study. In general, unless the melting of silicates inhibits the migration of iron sulfide melt in the open cracks (Tomkins et al., 2013; Kohout et al., 2018), within higher porosity models, shock-darkening could happen up to 60 GPa. However, the onset of shock-darkening still requires conditions that cannot be reproduced and, thus, requires further research.

### 4.7. Shock metamorphism

The observed melting in our models is shock-induced and our work disregarded effects related to heat diffusion (Moreau and Schwinger, 2019) and frictional heating (van der Bogert et al., 2003; see also Moreau et al., 2018 for more details) that happen during or after shock events, which may increase melting at lower shock stages (e.g. Stöffler et al., 1991, 2018; Rubin et al., 1997; Schmitt, 2000; Xie and Chen, 2016). Thus, our work cannot reproduce the melting of iron sulfides and metals observed at lower shock stages (C–S3 or C–S4)—mostly tributary to localized heating (Stöffler et al., 1991, 2018; Fritz et al., 2017). Only a small amount of iron sulfides (e.g. 2.8% of troilite at α: 0.012 in A2) melts at pressures right below 40 GPa, C–S5. The melting of olivine does happen at lower pressures, but very locally due to pore crushing. However, as stated above, the general amounts of total melting and post-shock temperatures are consistent with a number of previous studies (Stöffler et al., 1991, 2018; Bennett and McSween, 1996; Rubin et al., 1997; Schmitt, 2000; Xie and Chen, 2016), thus localized melting of metals and iron sulfides at lower shock stages is attributable to effects that we cannot, at this point, reproduce.

Compiling our findings from all 3–10% porous models (but pre-heated A1 model), for melting, melting features, post-shock temperatures, in all phases and bulk, in Fig. 12, we are able to relate our observations (green in Fig. 12) to the shock classification (Stöffler et al., 1991, 2018; Fritz et al., 2017):

1. The melting features of any phases at C–S5 and C–S6 are correlated to the observation of localized veins, dikes or melt pockets from localized hotspots.
2. The observation of plagioclase complete melting at C–S6 is correlated to the observation of shock melting of diaplectic glass. One can speculate whether the partial melting of plagioclase in our models, at C–S5, is linked to the presence of maskelynite.
3. The progressive melting of the bulk towards 70 GPa is correlated to the transition to whole-rock melt, C–S7 (75–90 GPa).
4. Post-shock temperatures of C–S5 and C–S6 are correlated to the estimated post-shock temperatures at the transition (Stöffler et al., 1991).

However, observations (red in Fig. 12) that do not correlate well with the shock classification, or have other implications for the shock classification are:

5. Eutectic melting occurring only from C–S5 in our models.

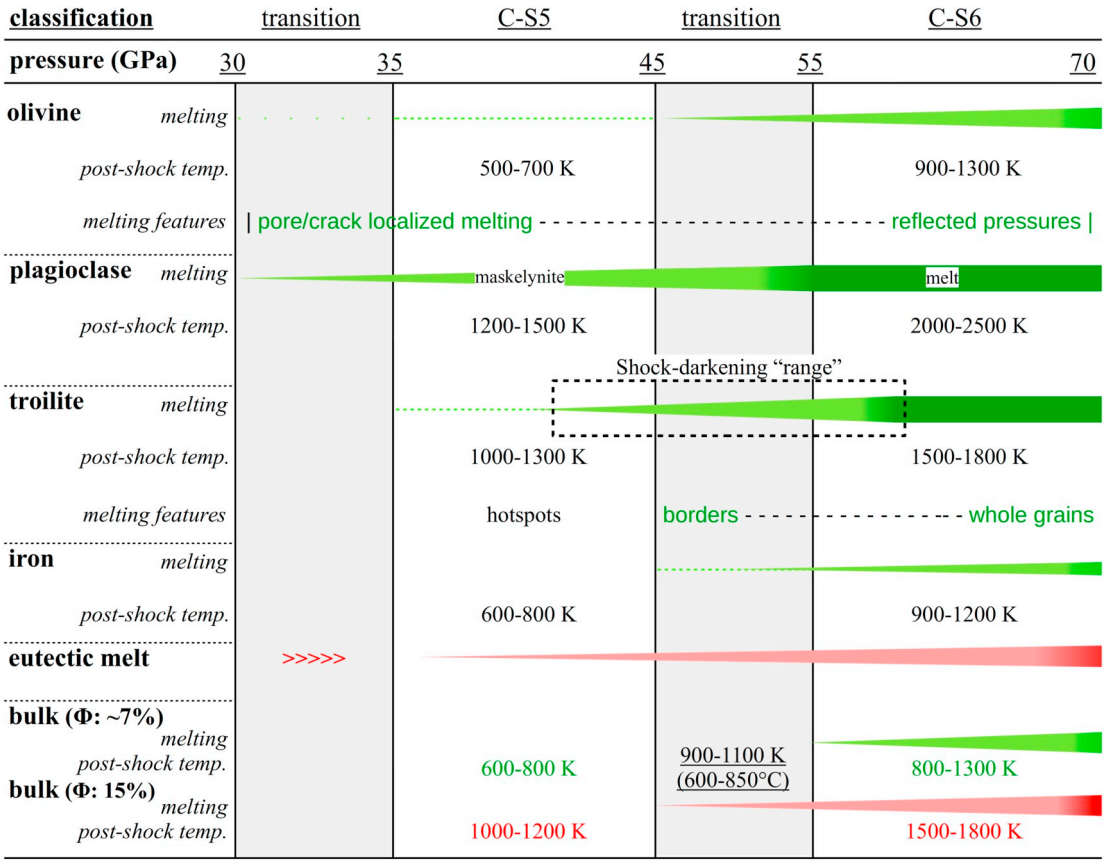


**Fig. 12.** Compilation of observations from the numerical models between 30 and 70 GPa at 3–10% porosity. The underlined texts originate from the shock metamorphism classification of Stöffler et al. (1991, 2018) and the pressures depicted at the top of the figure are either pressure estimations from Stöffler et al. (1991, 2018) or the nominal pressures in our models. Some details are provided for the 15% porosity model. The melt cones are an approximation of what is observed and plain rectangles depict very strong melting (troilite) or complete melting (plagioclase). Green texts/figures are correlated to the shock classification. Red texts/figures are either not correlated or are strongly implicated in the shock metamorphism classification (15% porosity model). (For interpretation of the references to color in this figure, the reader is referred to the web version of this article.)

6. Post-shock temperatures assessed for the 15% porous model A1 are not correlated to the classification, but this implies that the shock classification is dependent on the precursor material porosity for reaching any shock stages at lower pressures. This is also the case for pre-heated ordinary chondrites, but the decrease of required pressure of ~10–15 GPa to reach similar shock stages in our pre-heated model is correlated to the shock classification presented in Stöffler et al. (2018).

In general, our work illustrates well the possibility to study shock metamorphism using numerical modeling in terms of qualitative observations (e.g. the mapping of pressures, temperatures, and melting) and quantitative pressure, temperature, and melt estimates.

## 5. Conclusions

Using BSE images of ordinary and enstatite chondrites in the mesoscale models, we obtained results that correlate well with the transition between C–S5 and C–S6 in the classification of shock metamorphism of ordinary and enstatite chondrites. The transition from C–S5 to C–S6 (45–60 GPa), within the 3–10% porosity range, is dominated by the progressive and effective melting of plagioclase (reaching melt fraction of 1) and troilite (reaching melt fraction of ~0.6). The transition is accompanied by weak, but progressive, melting of olivine and iron starting at 50 GPa. We emphasize the shock stage classification dependence on porosity. An increase in porosity enhances the melting efficiency and shifts the onset of C–S5 to C–S6 transition to lower pressures. At 15% porosity, a pressure of ~10 GPa lower than that for a 5%-porosity lithology is required to reach an equivalent bulk melt fraction of 0.05. We also observed that:

1. Distribution of melt in troilite is grain-shape dependent.
2. Bulk post-shock temperatures are balanced by individual phases displaying heterogeneous post-shock temperatures.
3. Localized heating due to pore crushing can affect the whole bulk post-shock temperatures, and this is related to most of the localized P–T excursions in the shock stage classification. Heating and melting are also dependent on how open cracks are oriented to the shock wave.
4. Shock-darkening, dominated by troilite melting, ranges from 40 to 60 GPa, thus overlapping the transition between C–S5 and C–S6. However, at this pressure range, melting of highly porous silicates may inhibit shock-darkening.

## Acknowledgements

We gratefully acknowledge the developers of iSALE-2D, including Gareth Collins, Kai Wünnemann, Dirk Elbeshausen, Boris Ivanov and Jay Melosh. Some plots in this work were created with the pySALEPlot tool written by Tom Davison. The iSALE-Dellen version was used in this work (Collins et al., 2016).

## Funding

The work was supported by the Academy of Finland Project no. 285432 and within institutional support RVO 67985831 of the Institute of Geology of the Czech Academy of Sciences.

## Appendix A. Supplementary data

BSE images specifications and conversion (Fig. A1), result Tables A1–A9 for all models, additional information on the use of cylindrical symmetry (Table A11 and Fig. A2) and rounded grains (Table A11 and Fig. A3), additional peak shock melting tests (Fig. A4). Supplementary data to this article can be found online at https://doi.org/10.1016/j.icarus.2019.06.004. iSALE configuration files and scripts that allowed to carry out this research are available as modeling data (DOI: https://doi.org/10.5281/zenodo.2649931), as an open-source online data repository hosted at Zenodo (Moreau et al., 2019).

## References

Ahrens, T.J., Holland, K.G., Chen, G.Q., 1998. Shock temperatures and the melting point of iron. In: Schmidt, S.C., Dandekar, D.P., Forbes, J.W. (Eds.), Shock Compression of Condensed Matter. AIP Press, New York, pp. 133–136 Woodbuty.

Amsden, A.A., Ruppel, H.M., Hirt, C.W., 1980. SALE: A Simplified ALE Computer Program for Fluid Flow at All Speeds. Los Alamos National Laboratories Report LA-8095https://doi.org/10.2172/5176006. Los Alamos, New Mexico.

Bennett, M.E., McSween Jr., H.Y., 1996. Shock features in iron-nickel metal and troilite of L-group ordinary chondrites. Meteorit. Planet. Sci. 31, 255–264. https://doi.org/10.1111/j.1945-5100.1996.tb02021.x.

Bezaeva, N.S., Badjukov, D.D., Rochette, P., Gattacceca, J., Trukhin, V.I., Kozlov, E.A., Uehara, M., 2010. Experimental shock metamorphism of the L4 ordinary chondrite Saratov induced by spherical shock waves up to 400 GPa. Meteorit. Planet. Sci. 45, 1007–1020. https://doi.org/10.1111/j.1945-5100.2010.01069.x.

Bischoff, A., Schleiting, M., Patzek, M., 2018. Shock stage distribution of 2280 ordinary chondrites—can bulk chondrites with a shock stage of S6 exist as individual rocks? Meteorit. Planet. Sci. 1–14. https://doi.org/10.1111/maps.13208.

Bland, P.A., Collins, G.S., Davison, T.M., Abreu, N.M., Ciesla, F.J., Muxworthy, A.R., Moore, J., 2014. Pressure-temperature evolution of primordial solar system solids during impact-induced compaction. Nat. Commun. 5, 5451. https://doi.org/10.1038/ncomms6451.

Borg, J.P., Chhabildas, L.C., 2011. Three-dimensional dynamic loading simulations of sand. In: Air Force Research Laboratory, Munitions Directorate Report. Eglin AFB, FL, pp. 32542.

Britt, D.T., Pieters, C.M., 1989. Bidirectional reflectance characteristics of black chondrite meteorites (abstract). In: 20th Lunar Planet. Sci. Conf. Houston, Texas, pp. 109–110.

Britt, D.T., Pieters, C.M., 1994. Darkening in black and gas-rich ordinary chondrites: the spectral effects of opaque morphology and distribution. Geochim. Cosmochim. Acta 58, 3905–3919. https://doi.org/10.1016/0016-7037(94)90370-0.

Britt, D.T., Pieters, C.M., Petaev, M.I., Zaslavskaya, N.I., 1989. The Tsarev meteorite - petrology and bidirectional reflectance spectra of a shock-blackened L chondrite. In: 19th Lunar Planet. Sci. Conf. Houston, Texas, pp. 537–545.

Chen, M., El Goresy, A., 2000. The nature of maskelynite in shocked meteorites: not diaplectic glass but a glass quenched from shock-induced dense melt at high pressures. Earth Planet. Sci. Lett. 179, 489–502. https://doi.org/10.1016/S0012-821X(00)00130-8.

Clark, B.E., Hapke, B., Pieters, C., Britt, D., 2002. Asteroid space weathering and regolith evolution. In: Bottke, W., Cellino, A., Paolicchi, P., Binzel, R.P. (Eds.), Asteroid III. The University of Arizona Press, Tucson. Arizona, pp. 585–599.

Collins, G.S., Melosh, H.J., Ivanov, B.A., 2004. Modeling damage and deformation in impact simulations. Meteorit. Planet. Sci. 39, 217–231. https://doi.org/10.1111/j.1945-5100.2004.tb00337.x.

Collins, G.S., Melosh, H.J., Wünnemann, K., 2011. Improvements to the ε-α porous compaction model for simulating impacts into high-porosity solar system objects. Int. J. Impact Eng. 38, 434–439. https://doi.org/10.1016/j.ijimpeng.2010.10.013.

Collins, G.S., Wünnemann, K., Artemieva, N., Pierazzo, E., 2012. Numerical modelling of impact processes. In: Osinski, G.R., Pierazzo, E. (Eds.), Impact Cratering: Processes and Products. Blackwell Publishing Lt, pp. 254–270. https://doi.org/10.1002/9781118447307.ch17.

Collins, G.S., Elbeshausen, D., Wünnemann, K., Davison, T.M., Ivanov, B., Melosh, H.J., 2016. iSALE-Dellen Manual: A Multi-material, Multi-rheology Shock Physics Code for Simulating Impact Phenomena in Two and Three Dimensions. https://doi.org/10.6084/m9.figshare.3473690.

Crawford, D.A., Barnouin-Jha, O.S., Cintala, M.J., 2003. Mesoscale computational investigation of shocked heterogeneous materials with application to large impact craters (abstract #4119). In: 3rd Int. Conf. Large Meteor. Impacts, (Nördlingen, Germany, CD-ROM).

Davison, T.M., Collins, G.S., Bland, P.A., 2016. Mesoscale modeling of impact compaction of primitive solar system solids. Astrophys. J. 821, 17. https://doi.org/10.3847/0004-637X/821/1/68.

Davison, T.M., Derrick, J.G., Collins, G.S., Bland, P.A., Rutherford, M.E., Chapman, D.J., Eakins, D.E., 2017. Impact-induced compaction of primitive solar system solids: the need for mesoscale modelling and experiments. Procedia Eng 204, 405–412. https://doi.org/10.1016/j.proeng.2017.09.801.

DeMeo, F.E., Carry, B., 2014. Solar system evolution from compositional mapping of the asteroid belt. Nature 505, 629–634.

DeMeo, F.E., Binzel, R.P., Slivan, S.M., Bus, S.J., 2009. An extension of the Bus asteroid taxonomy into the near-infrared. Icarus 202, 160–180. https://doi.org/10.1016/j.icarus.2009.02.005.

Fritz, J., Greshake, A., Fernandes, V.A., 2017. Revising the shock classification of meteorites. Meteorit. Planet. Sci. 52, 1216–1232. https://doi.org/10.1111/maps.12845.

Gibbons, R.V., Ahrens, T.J., 1977. Effects of shock pressures on calcic plagioclase. Phys. Chem. Miner. 1, 95–107. https://doi.org/10.1007/BF00307982.

Güldemeister, N., Wünnemann, K., Durr, N., Hiermaier, S., 2013. Propagation of impact-induced shock waves in porous sandstone using mesoscale modeling. Meteorit. Planet. Sci. 48, 115–133. https://doi.org/10.1111/j.1945-5100.2012.01430.x.

Heymann, D., 1967. On the origin of hypersthene chondrites: ages and shock effects of black chondrites. Icarus 6, 189–221. https://doi.org/10.1016/0019-1035(67)90017-6.

Hirschmann, M.M., Ghiorso, M.S., Wasylenki, L.E., Asimow, P.D., Stolper, E.M., 1998. Calculation of peridotite partial melting from thermodynamic models of minerals and melts. I. Review of methods and comparison with experiments. J. Petrol. 39, 1091–1115. https://doi.org/10.1093/petroj/39.6.1091.

Hutchison, R., 2007. Meteorites: A Petrologic, Chemical and Isotopic Synthesis, 1st edition. Cambridge Planetary Science Series Cambridge University Press, UK.

Ivanov, B.A., 2005. Shock melting of permafrost on Mars: water ice multiphase equation of state for numerical modeling and its testing (abstract #1232). In: 36th Lunar Planet. Sci. Conf. League City, Texas.

Ivanov, B.A., Deniem, D., Neukum, G., 1997. Implementation of dynamic strength models into 2D hydrocodes: applications for atmospheric breakup and impact cratering. Int. J. Impact Eng. 20, 411–430. https://doi.org/10.1016/S0734-743X(97)87511-2.

Jaret, S.J., Woerner, W.R., Phillips, B.L., Ehm, L., Nekvasil, H., Wright, S.P., Glotch, T.D., 2015. Maskelynite formation via solid-state transformation: evidence of infrared and X-ray anisotropy. J. Geophys. Res. E: Planets 120, 570–587. https://doi.org/10.1002/2014JE004764.

Keil, K., Bell, J.F., Britt, D.T., 1992. Reflection spectra of shocked ordinary chondrites and their relationship to asteroids. Icarus 98, 43–53. https://doi.org/10.1016/0019-1035(92)90205-L.

Kohout, T., Donadini, F., Pesonen, L.J., Uehara, M., 2010. Rock magnetic studies of the Neuschwanstein EL6 chondrite - implications on the origin of its natural remanent magnetization. Geophysica 46, 3–19.

Kohout, T., Gritsevich, M., Grokhovsky, V.I., Yakovlev, G.A., Haloda, J., Halodova, P., Michallik, R.M., Penttilä, A., Muinonen, K., 2014. Mineralogy, reflectance spectra, and physical properties of the Chelyabinsk LL5 chondrite - insight into shock-induced changes in asteroid regoliths. Icarus 228, 78–85. https://doi.org/10.1016/j.icarus.2013.09.027.

Kohout, T., Haloda, J., Halodová, P., Meier, M.M.M., Maden, C., Busemann, H., Laubenstein, M., Caffee, M.W., Welten, K.C., Hopp, J., Trieloff, M., Mahajan, R.R., Naik, S., Trigo-Rodriguez, J.M., Moyano-Cambero, C.E., Oshtrakh, M.I., Maksimova, A.A., Chukin, A.V., Semionkin, V.A., Karabanalov, M.S., Felner, I., Petrova, E.V., Brusnitsyna, E.V., Grokhovsky, V.I., Yakovlev, G.A., Gritsevich, M., Lyytinen, E., Moilanen, J., Kruglikov, N.A., Ishchenko, A.V., 2017. Annama H chondrite—mineralogy, physical properties, cosmic ray exposure, and parent body history. Meteorit. Planet. Sci. 52, 1525–1541. https://doi.org/10.1111/maps.12871.

Kohout, T., Petrova, E.V., Yakovlev, G.A., Grokhovsky, V.I., Penttilä, A., Maturilli, A., 2018. Spherical shock experiments with Chelyabinsk meteorite: reflectance spectra changes with increasing shock (abstract #827). In: Eur. Planet. Sci. Congr. 12. pp. 16–21 (September 2018, Berlin, Germany).

Kovach, H.A., Jones, R.H., 2010. Feldspar in type 4-6 ordinary chondrites: metamorphic processing on the H and LL chondrite parent bodies. Meteorit. Planet. Sci. 45, 246–264. https://doi.org/10.1111/j.1945-5100.2010.01021.x.

Kring, D.A., Swindle, T.D., Britt, D.T., Grier, J.A., 1996. Cat Mountain: a meteoritic sample of an impact-melted asteroid regolith. J. Geophys. Res. Planets 101 (E12), 29353–29371. https://doi.org/10.1029/96JE03139.

Krupka, K.M., Hemingway, B.S., Borie, R.A., Kerrick, D.M., 1985. High-temperature heat capacities and derived thermodynamic properties of anthophyllite, diopside, dolomite, enstatite, bronzite, talc, tremolite and wollastonite. Am. Mineral. 70, 261–271.

Langenhorst, F., Deutsch, A., 1994. Shock experiments on pre-heated alpha-quartz and beta-quartz: I. Optical and density data. Earth Planet. Sci. Lett. 125, 407–420. https://doi.org/10.1016/0012-821x(94)90229-1.

Langenhorst, F., Hornemann, U., 2005. Shock experiments on minerals: basic physics and techniques. EMU Notes Mineral 7, 357–387.

Li, S., Wang, S., Li, X., Li, Y., Liu, S., Coulson, I.M., 2012. A new method for the measurement of meteorite bulk volume via ideal gas pycnometry. J. Geophys. Res. E: Planets 117, 7. https://doi.org/10.1029/2012JE004202.

Macke, R.J., Consolmagno, G.J., Britt, D.T., Hutson, M.L., 2010. Enstatite chondrite density, magnetic susceptibility, and porosity. Meteorit. Planet. Sci. 45, 1513–1526. https://doi.org/10.1111/j.1945-5100.2010.01129.x.

Mare, E.R., Tomkins, A.G., Godel, B.M., 2014. Restriction of parent body heating by metal-troilite melting: thermal models for the ordinary chondrites. Meteorit. Planet. Sci. 49, 636–651. https://doi.org/10.1111/maps.12280.

Melosh, H.J.J., Ryan, E.V.V., Asphaug, E., 1992. Dynamic fragmentation in impacts: hydrocode simulation of laboratory impacts. J. Geophys. Res. 97, 14735–14759. https://doi.org/10.1029/92JE01632.

Moreau, J., 2019. Shock-darkening in Ordinary Chondrites: Mesoscale Modelling of the Shock Process and Comparison With Shock-recovery Experiments. Ph.D. thesis. Unigrafia, Helsinki 60 pp. http://hdl.handle.net/10138/300084.

Moreau, J., Schwinger, S., 2019. 2-D heat diffusion in numerically shocked ordinary chondrites. In: 50th Lunar Planet. Sci. Conf, (abstract/e-poster no. 1025, The Woodlands, Texas, USA).

Moreau, J., Kohout, T., Wünnemann, K., 2017. Shock-darkening in ordinary chondrites: determination of the pressure-temperature conditions by shock physics mesoscale modeling. Meteorit. Planet. Sci. 52, 2375–2390. https://doi.org/10.1111/maps.12935.

Moreau, J., Kohout, T., Wünnemann, K., 2018. Melting efficiency of troilite-iron assemblages in shock-darkening: insight from numerical modeling. Phys. Earth Planet. Inter. 282, 25–38. https://doi.org/10.1016/j.pepi.2018.06.006.

[dataset]Moreau, J., Kohout, T., Wünnemann, K., Halodova, P., Haloda, J., 2019. Shock Physics Mesoscale Modeling of Shock Stage 5 and 6 in Ordinary and Enstatite Chondrites: Modeling Data. v1. https://doi.org/10.5281/zenodo.2649931.

Norton, O.R., 2002. The Cambridge Encyclopedia of Meteorites. Cambridge University Press, Cambridge, United Kingdom.

Ostertag, R., 1983. Shock experiments on feldspar crystals. J. Geophys. Res. Solid Earth 88 (S01), B364–B376.

Petrova, E.V., Grokhovsky, V.I., Kohout, T., Muftakhetdinova, R.F., Yakovlev, G.A., September 2018. Spherical shock experiments with Chelyabinsk meteorite: the experiment and textural gradient (abstract #709–1). Eur. Planet. Sci. Congr. 12, 16–21 (Berlin, Germany).

Riedel, W., Wicklein, M., Thoma, K., 2008. Shock properties of conventional and high strength concrete: experimental and mesomechanical analysis. Int. J. Impact Eng. 35, 155–171. https://doi.org/10.1016/j.ijimpeng.2007.02.001.

Rubin, A.E., 1992. A shock-metamorphic model for silicate darkening and compositionally variable plagioclase in CK and ordinary chondrites. Geochim. Cosmochim. Acta 56, 1705–1714. https://doi.org/10.1016/0016-7037(92)90236-C.

Rubin, A.E., 2015. Maskelynite in asteroidal, lunar and planetary basaltic meteorites: an indicator of shock pressure during impact ejection from their parent bodies. Icarus 257, 221–229. https://doi.org/10.1016/j.icarus.2015.05.010.

Rubin, A.E., Scott, E.R.D., Keil, K., 1997. Shock metamorphism of enstatite chondrites. . Geochim. Cosmochim. Acta 61, 847–858. https://doi.org/10.1016/S0016-7037(96)00364-X.

Russell, S.S., Zipfel, J., Folco, L., Jones, R.H., Grady, M.M., McCoy, T., Grossman, J.N., 2003. The Meteoritical Bulletin, No. 87, 2003 July. Meteorit. Planet. Sci. 38, A189–A248. https://doi.org/10.1111/j.1945-5100.2003.tb00328.x.

Schmieder, M., Kring, D.A., Swindle, T.D., Bond, J.C., Moore, C.B., 2016. The Gao-Guenie impact melt breccia—sampling a rapidly cooled impact melt dike on an H chondrite asteroid? Meteorit. Planet. Sci. 51 (6), 1022–1045. https://doi.org/10.1111/maps.12642.

Schmitt, R.T., 1995. Experimentelle und theoretische Untersuchungen zur Stoßwellenmetamorphose von gewöhnlichen Chondriten. Ph. D. Thesis. FB Geowissenschaften, WWU Münster (187 pp).

Schmitt, R.T., 2000. Shock experiments with the H6 chondrites Kernouvé: pressure calibration of microscopic shock effects. Meteorit. Planet. Sci. 35, 545–560.

Schmitt, R.T., Deutsch, A., Stöffler, D., 1994. Calculation of Hugoniot curves and post-shock temperatures for H- and L-chondrites. In: 25th Lunar Planet. Sci. Conf. Houston, Texas, USA, pp. 1209–1210.

Sharp, T.G., Xie, Z., de Carli, P.S., Hu, J., 2015. A large shock vein in L chondrite Roosevelt County 106: evidence for a long-duration shock pulse on the L chondrite parent body. Meteorit. Planet. Sci. 50 (11), 1941–1953. https://doi.org/10.1111/maps.12557.

Stöffler, D., 2000. Maskelynite confirmed as diaplectic glass: indication for peak shock pressures below 45 GPa in all Martian meteorites. In: 31th Lunar Planet. Sci. Conf, March. (abstract no. 1170).

Stöffler, D., Keil, K., Scott, E.R.D., 1991. Shock metamorphism of ordinary chondrites. Geochim. Cosmochim. Acta 55, 3845–3867. https://doi.org/10.1016/0016-7037(91)90078-J.

Stöffler, D., Ostertag, R., Jammes, C., Pfannschmidt, G., Gupta, P.S., Simon, S.B., Papike, J.J., Beauchamp, R.H., 1986. Shock metamorphism and petrography of the Shergotty achondrite. Geochim. Cosmochim. Acta 50 (6), 889–903.

Stöffler, D., Hamann, C., Metzler, K., 2018. Shock metamorphism of planetary silicate rocks and sediments: proposal for an updated classification system. Meteorit. Planet. Sci. 53, 5–49. https://doi.org/10.1111/maps.12912.

Tomioka, N., Kondo, H., Kunikata, A., Nagai, T., 2010. Pressure-induced amorphization of albitic plagioclase in an externally heated diamond anvil cell. Geophys. Res. Lett. 37, 5. https://doi.org/10.1029/2010GL044221.

Tomkins, A.G., 2009. What metal-troilite textures can tell us about post-impact metamorphism in chondrite meteorites. Meteorit. Planet. Sci. 44, 1133–1149. https://doi.org/10.1111/j.1945-5100.2009.tb01213.x.

Tomkins, A.G., Weinberg, R.F., Schaefer, B.F., Langendam, A., 2013. Disequilibrium melting and melt migration driven by impacts: implications for rapid planetesimal core formation. Geochim. Cosmochim. Acta 100, 41–59. https://doi.org/10.1016/j.gca.2012.09.044.

Trieloff, M., Korochantseva, E.V., Bulkin, A.I., Hopp, J., Ivanova, M.A., Korochantsev, A.V, 2017. The Chelyabinsk meteorite: thermal history and variable shock effects recorded by the $^{40}$Ar-$^{39}$Ar system. Meteorit. Planet. Sci. 53 (3), 343–358. https://doi.org/10.1111/maps.13012.

van der Bogert, C.H., Schultz, P.H., Spray, J.G., 2003. Impact-induced frictional melting in ordinary chondrites: a mechanism for deformation, darkening, and vein formation. Meteorit. Planet. Sci. 38, 1521–1531. https://doi.org/10.1111/j.1945-5100.2003.tb00255.x.

Van Schmus, W.R., Ribbe, P.H., 1968. The composition and structural state of feldspar from chondritic meteorites. Geochim. Cosmochim. Acta 32, 1327–1342. https://doi.org/10.1016/0016-7037(68)90032-X.

Wang, D., Chen, M., 2006. Shock-induced melting, recrystallization, and exsolution in plagioclase from the Martian lherzolitic shergottite GRV 99027. Meteorit. Planet. Sci. 41, 519–527. https://doi.org/10.1111/j.1945-5100.2006.tb00479.x.

Wang, B., Miao, B., Wang, J., Zhang, J., 2011. Shock effects and the classification of H-chondrites from the Grove Mountains, East Antarctica: implications for the shock history of H-chondrite parent bodies. Adv. Polym. Sci. 22, 81–91. https://doi.org/10.3724/SP.J.1085.2011.00081.

Wünnemann, K., Collins, G.S., Melosh, H.J., 2006. A strain-based porosity model for use in hydrocode simulations of impacts and implications for transient crater growth in porous targets. Icarus 180, 514–527. https://doi.org/10.1016/j.icarus.2005.10.013.

Wünnemann, K., Collins, G.S., Osinski, G.R., 2008. Numerical modelling of impact melt production in porous rocks. Earth Planet. Sci. Lett. 269, 529–538. https://doi.org/10.1016/j.epsl.2008.03.007.

Xie, X., Chen, M., 2016. Suizhou Meteorite: Mineralogy and Shock Metamorphism. Springer-Verlag Berlin and Heidelberg. https://doi.org/10.1007/978-3-662-48479-1.